ICARUS 106, 442–463 (1993)

Methane Photochemistry on Neptune: Ethane and Acetylene Mixing Ratios and Haze Production

PAUL N. ROMANI

Mail Code 693, NASA–Goddard Space Flight Center, Greenbelt, Maryland 20771
E-mail: ys2pr@viris.dnet.nasa.gov

JAMES BISHOP

Computational Physics Inc., 2750 Prosperity Avenue, Suite 600, Fairfax, Virginia 22031

BRUNO BÉZARD

Observatoire de Paris, Section de Meudon, Département de Recherche Spatiale, 92195 Meudon, France

AND

SUSHIL ATREYA

Department of Atmospheric, Oceanic and Space Sciences, University of Michigan, Space Research Building, Ann Arbor, Michigan 48109-2143

Received October 1, 1992; revised September 16, 1993

We have used a one-dimensional methane photochemical model to analyze Voyager observations of hydrocarbons and hazes in the stratosphere of Neptune. Voyager IRIS spectra provide information about the global average C_2H_2 and C_2H_6 mixing ratios for $p > 0.1$ mbar. The UVS lightcurves provide constraints on CH_4 and C_2H_4 in addition to C_2H_2 and C_2H_6 but only at the solar occultation latitudes and for lower pressures. The model-predicted hydrocarbons are very sensitive to the height profile of the eddy diffusion coefficient (K). For both data sets K varying inversely with the atmospheric number density to some power produced poor results. Good agreement with the data requires that K be weak in the lower stratosphere ($K \approx 2 \times 10^3$ cm^2 sec^{-1} for $p \gtrsim 2$ mbar) but fairly vigorous in the upper stratosphere ($K \geq 5 \times 10^7$ cm^2 sec^{-1} for $p \lesssim 0.5$ mbar), i.e., a rapidly mixed upper stratosphere overlying a stagnant lower stratosphere with a rapid transition in between. The model C_2H_6 and C_2H_2 mixing ratios are also sensitive to the reaction rate constants of $C_2H_4 + H$ and $CH_3 + C_2H_3$. Notably, we must use the present upper limit for the $C_2H_4 + H$ rate to best fit the model results to the observations. We are able to reproduce the IRIS C_2H_2 and C_2H_6 emission features well, less so the UVS occultation lightcurves. Since the transport of C_2H_2, C_2H_6, and other hydrocarbons produced from methane photolysis out of the stratosphere is by ice haze formation and sedimentation, we compared model haze predictions to PPS and IRIS observations. For solar maximum fluxes (Voyager encounter conditions) the model mass production rate is 1×10^{-14} g cm^2 sec^{-1}. C_2H_6 is the dominant haze component (75%), with the remainder coming from C_2H_2 and C_3 and C_4 compounds. Balancing the above haze production rate by the sedimentation rate for 0.25-μm radius particles (upper limit to particle radius from PPS observations) yields a total haze column burden slightly above the PPS upper limit. However, lifetime analysis indicates that the model haze production rate should be averaged over solar minimum and maximum conditions. Under these conditions the model haze density is consistent with the PPS data. The predicted C_4H_2 and C_2H_6 haze column densities are consistent with the lack of ice signatures in the IRIS spectra.

I. INTRODUCTION

Methane (CH_4) and its photochemical products acetylene (C_2H_2) and ethane (C_2H_6) have been observed in emission in the infrared from Neptune's stratosphere for over 10 years (see references in Orton and Appleby 1984, and Kostiuk *et al.* 1992). The retrieved mole fractions of these species are much greater than their respective saturation mixing ratios at the tropopause. This, coupled with observational evidence of a lower stratospheric haze ($p > 5$ mbar) on Neptune (see, e.g., Baines and Smith 1990, Hammel *et al.* 1989), naturally led to the speculation that these and potentially more complex hydrocarbons were the source for the haze.

An understanding of these hydrocarbons and hazes is important to an understanding of the carbon cycle in the stratosphere of Neptune. Carbon, in the form of methane,

0019-1035/93 $5.00

is transported from the troposphere into the stratosphere, where it is converted into C_2 and higher-order organics by photolysis and subsequent chemistry. The photolysis products are then transported downward to the lower stratosphere, where they form the hazes. It is then the sedimentation of the haze particles into the troposphere that finally removes carbon from the stratosphere. Thus, in a steady-state situation, the photolytic destruction of methane determines the haze production rate.

Prior to the Voyager 2 encounter with Neptune, Romani and Atreya (1989) made predictions about the C_2H_6 and C_2H_2 mixing ratios and haze production from methane photochemistry. They used a one-dimensional methane photochemical model which included a condensation loss process for acetylene, ethane, and, diacetylene (C_4H_2). This type of model needs basic input information about the thermal structure and the methane mixing ratio in the lower stratosphere of Neptune. Postencounter we now have better/new information about these quantities. The Voyager Ultraviolet Spectrometer (UVS), Infrared Interferometer Spectrometer and Radiometer (IRIS), and Radio Science Subsystem (RSS) instruments returned data on the thermal structure. Analysis of the Voyager UVS occultation data, and reanalysis of groundbased data, has yielded constraints on the methane mixing ratio in the lower stratosphere (Bishop *et al.* 1992, Baines and Hammel 1992, Orton *et al.* 1992).

In this paper we update the work of Romani and Atreya (1989) by using an expanded photochemical model and making use of post-Voyager encounter information about the background atmosphere. We first compare the model hydrocarbon vapor phase mixing ratios to Voyager IRIS and UVS observations. In addition to the photochemical reactions, the model ethane and acetylene mixing ratios are very sensitive to the choice of the eddy diffusion coefficient, K (see Bézard *et al.* 1991 and Bishop *et al.* 1992). We have information about K near the tropopause from analysis of the thermal structure observed by IRIS (Conrath *et al.* 1991). Analysis of the Voyager UVS occultation data has yielded constraints about the eddy diffusion coefficient in the microbar region (Parkinson *et al.* 1990, Bishop *et al.* 1992). The ethane and acetylene emission observed by Voyager IRIS originates in the 3- to 4.0 $\times 10^{-2}$ – mbar region (Bézard *et al.* 1991)—intermediate to the first two observations. Thus, with respect to the model photochemical reaction system, we can use the model and all of these data sets to derive an altitude profile for the eddy diffusion coefficient. The model also predicts a hydrocarbon ice haze production rate. Since haze production is not a directly observed quantity we must convert it into a haze column density before comparing it to observations. We test our model haze predictions against Voyager IRIS and Photopolarimeter Subsystem (PPS) observations (Pryor *et al.* 1992) as well as groundbased observations (Baines and Hammel 1992).

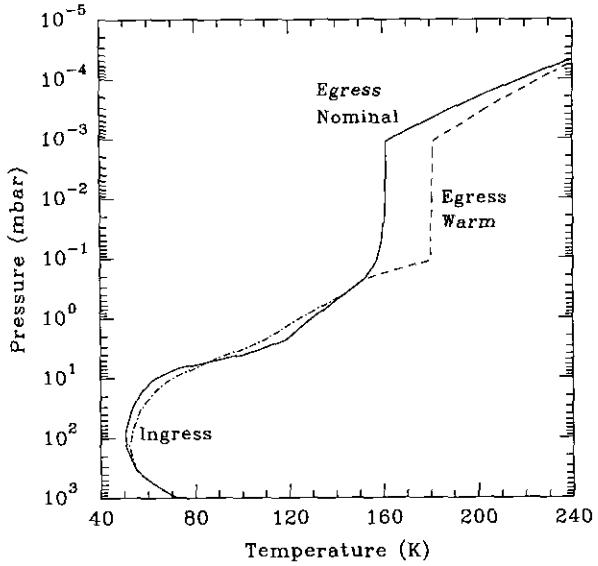

FIG. 1. The thermal profiles used in the photochemical model and data analysis. They are based in part upon Voyager egress (49°S) and ingress (61°N) occultation data. The egress warm profile is 20 K warmer in the 10^{-1}- to 10^{-3}-mbar region than the egress nominal profile. For pressures less than 0.2 mbar the ingress and egress nominal profiles are identical. See text for details.

The paper is organized into the following sections. The model atmospheres and photochemical model used in this study are described in Section II. In Section III, the model predicted vapor phase mixing ratios are compared to the Voyager 2 observations. Haze results are discussed in Section IV. Lastly, we summarize all results and discuss future work in Section V.

II. MODEL DESCRIPTION

II.A. Model Atmosphere

The thermal structures used in this study are shown in Fig. 1. They are taken from Bishop *et al.* (1992) and we briefly summarize them here. For pressures greater than ≈3 mbar they are based upon either the RSS ingress or egress occultation (Lindal *et al.* 1990), while for pressures less than ≈0.03 μbar they are based upon the UVS ingress occultation (Broadfoot *et al.* 1989). The RSS data were rescaled to an He mole fraction of 0.19 (Conrath *et al.* 1991). The recent reanalysis of the RSS occultations and UVS occultations (Lindal 1992 and Yelle *et al.* 1993, respectively) have minimal effect upon these thermal profiles. To bridge the RSS–UVS information gap we used temperature information from the analysis of stellar occultations by Neptune. For the nominal profile we relied upon the analysis of a central flash by Hubbard *et al.*

(1987) with temperatures also rescaled to an He mole fraction of 0.19. (Marten *et al.* 1993 have recently proposed that the N_2 mixing ratio on Neptune might be as large as 0.3% with a commensurate reduction in the He mole fraction to 0.15. This does not affect the thermal structure since it is sensitive mainly to the mean molecular weight of the atmosphere which would remained unchanged under these circumstances.) The nominal egress profile is very similar to the one used by Bézard *et al.* (1991) in their analysis of the IRIS observations of C_2H_6 and C_2H_2, because it is based upon the same sources. Bézard *et al.* (1991), however, assumed the atmosphere to be isothermal for all pressures less than 0.1 mbar. In addition to the nominal profiles we also used an egress "warm" profile. The warm profile is ≈20 K warmer in the region between 10^{-1} and 10^{-3} mbar but is still within the range in temperatures deduced from stellar occultation observations (Hubbard *et al.* 1985, French *et al.* 1985, Roques *et al.* 1992). Our motivation for including a warm profile is based upon our choice for the methane mixing ratio in the lower stratosphere (see below).

These thermal profiles were used to test the sensitivity of the data analysis and model results to changes in the thermal structure of the atmosphere. Bézard *et al.* (1991) and Bishop *et al.* (1992) discuss how changes in atmospheric thermal structure affect interpretation of the IRIS and UVS observations. The model results are sensitive to temperature through the temperature dependence of the reaction rate constants and the vapor pressures in the condensation loss process (see Section II.E). Both of these processes are exponentially dependent upon temperature. The model results are also sensitive to the temperature–pressure structure in the condensation region. Changing the thermal gradient changes the pressure level where condensation occurs in the results, while the temperature remains essentially unchanged because of the strong temperature dependence of the condensation loss rate. This affects comparison of the pressure where condensation first occurs in this study to other work. Changes in the thermal structure can also affect the relative production rates of the condensing hydrocarbons. For example, C_4H_2 is a daughter product of C_2H_2 and thus its production is inhibited by C_2H_2 condensation. The thermal structure of the atmosphere controls the relative placement of the C_2H_2 and C_4H_2 condensation levels and influences the fraction of C_2H_2 that is converted to C_4H_2.

Since the photochemical model is one-dimensional it implicitly assumes a global average atmosphere in both longitude and latitude. We have also chosen solar flux conditions to be representative of global average conditions (see Section II.C). It is then fair to ask whether these thermal profiles are representative of global average conditions. We realize that they rely heavily upon the RSS occultations (ingress 62°N, egress 45°S) and the UVS ingress occultation (≈RSS ingress). It can be argued that from comparison of the RSS profiles to IRIS data sensitive to the tropopause temperature (Conrath *et al.* 1991) that the egress model atmosphere is too cold to be a global average since it occurred in a cold latitude band. However, we can see in Fig. 1 that while the ingress profile is warmer than the egress at the tropopause, they cross and that for $p < 5$ mbar the egress profile is warmer. The RSS data also provide the only information we have on the thermal structure in the region we expect the hydrocarbons to condense.

II.B Methane Mixing Ratio in the Lower Stratosphere

In Romani and Atreya (1989) the methane mixing ratio in the lower stratosphere was 2%. This was based upon pre-Voyager radiative transfer models which predicted the stratospheric thermal structure and methane 7.8-μm radiances from Neptune (e.g., Orton *et al.* 1990). Even the nominal thermal profiles given above are warmer than the preencounter model atmospheres and thus require a lower methane mixing ratio to reproduce groundbased observations. Most recently Orton *et al.* (1992) from reanalysis of the data given in Orton *et al.* (1990) have retrieved a nominal stratospheric CH_4 mixing ratio of 7.5×10^{-4} (for a temperature of 168 K near 1–10 μbars). Independently, from analysis of methane absorption features, Baines and Hammel (1992) have derived a nominal value of 3.5×10^{-4}. Even lower CH_4 mole fractions, on the order of 10^{-4}, are possible (from analysis of Voyager UVS occultation data Bishop *et al.* 1992). For this study we adopted a value of the methane mixing ratio at the tropopause of 10^{-4}. Since it is possible to get better agreement between the UVS and groundbased IR measurements with the warm model atmosphere we also used it as input to the photochemical model.

However, changing the CH_4 mixing ratio in the lower stratosphere from 2% to 10^{-4} causes much less proportional changes in the model acetylene and ethane and only alters the total haze production by a factor of two. This is because methane photolysis and the subsequent haze production is primarily a photon-limited process. As discussed in Romani and Atreya (1989), the methane cross section is large enough at Lyman α (where the majority of photolyzing photons are) that unit optical depth, $\tau = 1$, is reached hundreds of kilometers above the tropopause even for a mixing ratio of 10^{-4}. Changing the methane mixing ratio shifts the $\tau = 1$ level to a different pressure level in the stratosphere. This affects the subsequent chemistry and the haze production because it changes the temperature and number density where the photochemistry takes place which then in turn alters the reaction rates and fractionation between three and two-body reaction pathways.

II.C. Solar Flux

To be consistent with the Voyager UVS observations we used solar maximum fluxes (5.0×10^{11} photons cm^{-2} sec^{-1} at 1 AU at Lyman α). The fluxes were diurnally averaged and the solar zenith angle was 50°. This is representative of global average conditions. As pointed out by Strobel *et al.* (1990) in their study of methane photochemistry on Triton, the LISM (local interstellar medium) Lyman α intensity leads to a methane dissociation rate comparable to the diurnal average solar rate at Neptune's distance from the Sun. Since the rotation period is much shorter than the photodissociation lifetimes, the LISM emissions averaged over the entire sky should be used in estimating atmospheric photolysis rates. Using the LISM Lyman α measurements acquired by the Voyager UVS near the time of encounter, the effective sky-summed intensity as seen from an altitude z within the stratosphere is approximately $1.6 \times 10^8\ e^{(-\tau/\cos(50°))}$ photons cm^{-2} sec^{-1}.

II.D. Photochemical Model

The basic numerical technique is the same as in Romani and Atreya (1989). The model assumes a steady-state condition and a horizontally averaged atmosphere so the continuity equation for the ith species becomes

$$\frac{-d\Phi_i}{dz_i} + P_i - L_i = 0, \tag{1}$$

where Φ_i is the flux of the species in molecules cm^{-2} sec^{-1}, z is the altitude and P_i and L_i are respectively the chemical production and chemical loss rate of the species in molecules cm^{-3} sec^{-1}. In Table I we list the species presently in our model. If the chemical lifetime of a species is much smaller than the transport time, then the flux term in Eq. (1) can be neglected and the mixing ratio of the species is solved for by equating chemical production to loss at each level in the model. If the species is not in photochemical equilibrium, then the full continuity equation must be solved. These coupled continuity equations are then finite differenced and solved by using an iterative Newton–Raphson technique. A convergence criteria of 1% was used for all cases. At the lower boundary (tropopause) fixed-point boundary conditions are used. Due to the rapid condensation sink near the lower boundary our results are not sensitive to the chosen lower boundary values. At the upper boundary for the hydrocarbon species we assume diffusive equilibrium, i.e., zero flux, while for atomic hydrogen we assume a net downward flux of 4×10^7 molecules cm^{-2} sec^{-1}. This flux represents H production by solar EUV (photons and photoelectrons) above the upper boundary. It was derived by scaling the observed flux at Jupiter ($\sim 1.3 \times 10^9$, Gladstone 1983) during the time of the Voyager encounters in 1979 to Neptune (both occurred during solar maximum periods).

Both eddy and molecular diffusion are included in the flux term in Eq. (1) since the model includes both the well mixed portion of the atmosphere and the region of diffusive separation. The molecular diffusion coefficients for the hydrocarbons and atomic hydrogen in H_2 and He are either for Marrero and Mason (1972) and the references contained therein, or are estimated in the manner of Fuller, Schettler, and Giddings as given in Reid *et al.* (1977). These background gas dependent diffusion coefficients are then combined to produce diffusion coefficients appropriate to the model atmosphere.

In a one-dimensional model all of the dynamics collapses into a single parameter—the eddy diffusion coefficient, K. The strength of K is representative of the amount of vertical mixing in the atmosphere, from whatever source: waves or mass motion (see Holton and Schoeberl 1988). We treat this as a free parameter to be constrained by model–observation comparison. Thus we defer discussion of the K profiles to Section III.

The photochemical reactions are listed in Table II and the major pathways are diagrammed in Fig. 2. A complete list of the rate constants used and their references is available upon request (from P. Romani). The number of reactions have been expanded since the Bézard *et al.* (1991) study (NB that Kostiuk *et al.* 1992 used the same chemical scheme as Bézard *et al.* 1991). Specifically they are R2, R3, R22, R24, R25, R41, R44, R47, and R48. The most important ones are those which make the C_3 and C_4 hydrocarbons (R22, R24, R25, R41, R44, and R48) because inclusion of them results in lowered C_2 production. Presently, the model is complete through the C_1 and C_2 hydrocarbons, with only limited C_3 and C_4 hydrocarbon chemistry. In general we only include the production of C_3 and C_4 compounds. The affect on the model is the equivalent to assuming that subsequent photochemistry of these compounds does not then alter the C_1 and C_2 distributions. This, however, may not be the case. Moses (1991), using a model which includes more C_3 and C_4 reactions than ours, found that C_3 and C_4 compounds regenerated C_1 and C_2 species 80–95% of the time. To investigate this further we ran our model with a solar flux, model atmosphere, and K profile similar to those used in Fig. 5 of Moses *et al.* (1992). The two model C_2H_2 and C_2H_6 mixing ratios agreed to within an average of 35% in the 1–0.1-mbar region (outside the condensation region of these species).

II.E. Haze Production

The handling of the condensation loss process of C_4H_2, C_2H_2, and C_2H_6 from the vapor phase is the same as in Romani and Atreya (1989). Here we give a discussion of

TABLE I
Chemical Species

Chemical formula	Name	Chemical formula	Name
CH_4	Methane	a-C_3H_4, $CH_2C_2H_2$	Allene[b]
CH_3	Methyl	C_3H_5	Propenyl[b]
$^3CH_2$	Triplet methylene (ground state)	C_3H_6	Propene, a.k.a. propylene[b]
$^1CH_2$	Singlet methylene (excited state)[a]	C_3H_8	Propane[b]
CH	Methylidyne[a]	C_4H	Butadiynyl[a]
C	Atomic carbon[b]	C_4H_2	Diacetylene, a.k.a. 1,3-butadiyne
C_2	Diatomic carbon[a]	C_4H_2**	Excited metastable diacetylene[a]
C_2H	Ethynyl[a]	C_4H_3[a]	
C_2H_2	Acetylene	C_4H_4	Vinyl acetylene[b]
C_2H_3	Vinyl	C_4H_6	1,3-Butadiene[b]
C_2H_4	Ethylene	1-C_4H_8	1-Butene[b]
C_2H_5	Ethyl	C_4H_{10}	Butane[b]
C_2H_6	Ethane	C_6H_2	Triacetylene, a.k.a. hexatriyne[b]
C_3H_2	Propynylidene	C_8H_2	Tetraacetylene, a.k.a. octatetrayne[b]
p-C_3H_4, CH_3C_2H	Propyne, a.k.a. methyl acetylene[a]	H	Atomic hydrogen

[a] Species assumed to be in photochemical equilibrium.
[b] Species has chemical production only.

the loss process in more detail. The loss process is based upon the diffusive growth rate of ice crystals—vapor phase molecules strike an already existing ice crystal and stick to it. The diffusive mass growth rate (gm sec^{-1}) of an individual ice crystal is taken from Pruppacher and Klett (1980),

$$\frac{dm}{dt} = \frac{4\pi a s Vp D' M}{RT}, \tag{2}$$

where a is the crystal radius, s is the supersaturation, T is the temperature in degrees Kelvin, R is the universal gas constant, D' is the molecular diffusion coefficient of the condensing species corrected for gas kinetic effects for small crystals, and Vp and M are respectively the vapor pressure and the molecular weight of the condensing species. As written, Eq. (2) neglects the effects of latent heat release (compare to Eq. (13-71) in Pruppacher and Klett, 1980, p. 448). Under the conditions in our study this term proved to be negligibly small.

The relationship between D, the standard molecular diffusion coefficient, and D' is

$$D' = \frac{D}{[a/(a+\lambda)] + [D/(a\alpha)]\sqrt{(2\pi M)/(RT)}}, \tag{3}$$

where λ is the mean free path of the atmospheric molecules and α is the sticking efficiency. In our models we assumed a nominal sticking efficiency of unity. For small crystals the second term in the denominator of Eq. (3) dominates and the crystal grows proportional to a^2; for large crystals the first term dominates and D' approaches the limit of D and the crystal grows as only a. If we had assumed nonspherical crystals, then a would be replaced by the capacitance of the crystal, C. (The problem of diffusive growth is directly analogous to the problem of the electrostatic potential, see Pruppacher and Klett 1980, p. 448–450.) For crystals of approximately equal size, but different shape, the variability of C is within a factor of 3.

Equation (2) is the mass growth rate of an individual crystal. For the photochemical model we need a loss rate in molecules cm^{-3} sec^{-1}, thus we need to multiply Eq. (2) by the reciprocal of the molecular weight and the number density of ice crystals. To calculate the number density of the ice crystals we assumed that all downward transport of a condensing hydrocarbon through the tropopause was by ice crystal sedimentation. Since our model is a steady-state model the net photochemical column production rate of each species is balanced by the downward flux of its aerosols. The aerosol flux is equivalent to the column density of aerosols times a reciprocal life-

TABLE II
Photochemical Reactions

Reaction			Number
$CH_4 + h\nu$	→	$^3CH_2 + 2\,H$	J1A
	→	$^1CH_2 + H_2$	J1B
	→	$CH + H + H_2$	J1C
$C_2H_2 + h\nu$	→	$C_2H + H$	J2A
	→	$C_2 + H_2$	J2B
$C_2H_4 + h\nu$	→	$C_2H_2 + H_2$	J3A
	→	$C_2H_2 + 2\,H$	J3B
$C_2H_6 + h\nu$	→	$C_2H_2 + 2\,H_2$	J4A
	→	$C_2H_4 + 2\,H$	J4B
	→	$CH_4 + {}^1CH_2$	J4C
	→	$C_2H_4 + H_2$	J4D
	→	$2\,CH_3$	J4E
$C_4H_2 + h\nu$	→	$C_4H + H$	J5A
	→	$C_2H_2 + C_2$	J5B
	→	$2\,C_2H$	J5C
	→	$C_4H_2^{**}$	J5D
$C_4H_2^{**}$	→	$C_4H_2 + h\nu$	J6A
$CH_3 + h\nu$	→	$^1CH_2 + H$	J7A
$CH + H_2 + M^a$	→	$CH_3 + M^a$	R1
$CH + H_2$	→	$^3CH_2 + H$	R2
$CH + H$	→	$C + H_2$	R3
$CH + CH_4$	→	$C_2H_4 + H$	R4
$CH + C_2H_2$	→	$C_3H_2 + H$	R5
$CH + C_2H_4$	→	$p\text{-}C_3H_4 + H$	R6
$CH + C_2H_4$	→	$a\text{-}C_3H_4 + H$	R7
$CH + C_2H_6$	→	Products	R8
$^1CH_2 + H_2$	→	$CH_3 + H$	R9
$^1CH_2 + H_2$	→	$^3CH_2 + H_2$	R10
$^1CH_2 + CH_4$	→	$2\,CH_3$	R11
$^1CH_2 + CH_4$	→	$^3CH_2 + CH_4$	R12
$^3CH_2 + H + M^a$	→	$CH_3 + M^a$	R13
$^3CH_2 + H$	→	$CH + H_2$	R14
$^3CH_2 + {}^3CH_2$	→	$C_2H_2 + 2\,H$	R15
$^3CH_2 + CH_3$	→	$C_2H_4 + H$	R16
$^3CH_2 + C_2H_2$	→	Products	R17
$^3CH_2 + C_2H_3$	→	$CH_3 + C_2H_2$	R18
$^3CH_2 + C_2H_5$	→	$CH_3 + C_2H_4$	R19
$CH_3 + H + M^a$	→	$CH_4 + M^a$	R20
$2\,CH_3 + M^a$	→	$C_2H_6 + M^a$	R21
$CH_3 + C_2H_3 + M^a$	→	$C_3H_6 + M^a$	R22
$CH_3 + C_2H_3$	→	$CH_4 + C_2H_2$	R23
$CH_3 + C_2H_3$	→	$C_3H_5 + H$	R24
$CH_3 + C_2H_5 + M^a$	→	$C_3H_8 + M^a$	R25
$CH_3 + C_2H_5$	→	$CH_4 + C_2H_4$	R26
$C_2 + H_2$	→	$C_2H + H$	R27
$C_2 + CH_4$	→	$C_2H + CH_3$	R28
$C_2H + H_2$	→	$C_2H_2 + H$	R29
$C_2H + H + M^a$	→	$C_2H_2 + M^a$	R30
$C_2H + CH_4$	→	$C_2H_2 + CH_3$	R31
$C_2H + C_2H_2$	→	$C_4H_2 + H$	R32
$C_2H + C_2H_4$	→	$C_4H_4 + H$	R33
$C_2H + C_2H_6$	→	$C_2H_2 + C_2H_5$	R34
$C_2H + C_4H_2$	→	$C_6H_2 + H$	R35
$C_2H_3 + H_2$	→	$C_2H_4 + H$	R36
$C_2H_3 + H$	→	$C_2H_2 + H_2$	R37
$C_2H_3 + CH_4$	→	$CH_3 + C_2H_4$	R38
$2\,C_2H_3 + M^a$	→	$C_4H_6 + M^a$	R39
$2\,C_2H_3$	→	$C_2H_4 + C_2H_2$	R40
$C_2H_3 + C_2H_5 + M^a$	→	$1\text{-}C_4H_8 + M^a$	R41
$C_2H_3 + C_2H_5$	→	$2\,C_2H_4$	R42
$C_2H_3 + C_2H_5$	→	$C_2H_2 + C_2H_6$	R43
$C_2H_3 + C_2H_5$	→	$CH_3 + C_3H_5$	R44
$C_2H_5 + H + M^a$	→	$C_2H_6 + M^a$	R45
$C_2H_5 + H$	→	$2\,CH_3$	R46
$C_2H_5 + H$	→	$C_2H_4 + H_2$	R47
$2\,C_2H_5 + M^a$	→	$C_4H_{10} + M^a$	R48
$2\,C_2H_5$	→	$C_2H_6 + C_2H_4$	R49
$p\text{-}C_3H_4 + H + M^a$	→	$C_3H_5 + M^a$	R50
$p\text{-}C_3H_4 + H$	→	$CH_3 + C_2H_2$	R51
$C_4H + H_2$	→	$C_4H_2 + H$	R52
$C_4H + H + M^a$	→	$C_4H_2 + M^a$	R53
$C_4H + CH_4$	→	$C_4H_2 + CH_3$	R54
$C_4H + C_2H_2$	→	$C_6H_2 + H$	R55
$C_4H + C_2H_6$	→	$C_4H_2 + C_2H_5$	R56
$C_4H_3 + H$	→	$C_4H_2 + H_2$	R57
$C_4H_3 + H$	→	$2\,C_2H_2$	R58
$C_4H + C_4H_2$	→	$C_8H_2 + H$	R59
$C_4H_2^{**} + C_4H_2$	→	$C_8H_2 + H_2$	R60
$2\,H + M^a$	→	$H_2 + M^a$	R61
$H + C_2H_2 + M^a$	→	$C_2H_3 + M^a$	R62
$H + C_2H_4 + M^a$	→	$C_2H_5 + M^a$	R63
$H + C_4H_2 + M^a$	→	$C_4H_3 + M^a$	R64

[a] M denotes a background atmosphere molecule.

time. For lifetimes we used the time it takes for the aerosols to fall from their respective condensation levels to the tropopause. Thus we have

$$N_{crys} = P_{col}\,\tau_{fall} \tag{4}$$

where N_{crys} is the column density of ice crystals, P_{col} is the photochemical column production rate of the crystals, and τ_{fall} is the fall time. In the model the fall times were calculated by summing the fall times of constant-radius particles at 1 km resolution (1/10 scale height or better) from the condensation level to the tropopause using

$$\tau_{fall} = \sum \frac{\Delta z}{U_\infty} \tag{5}$$

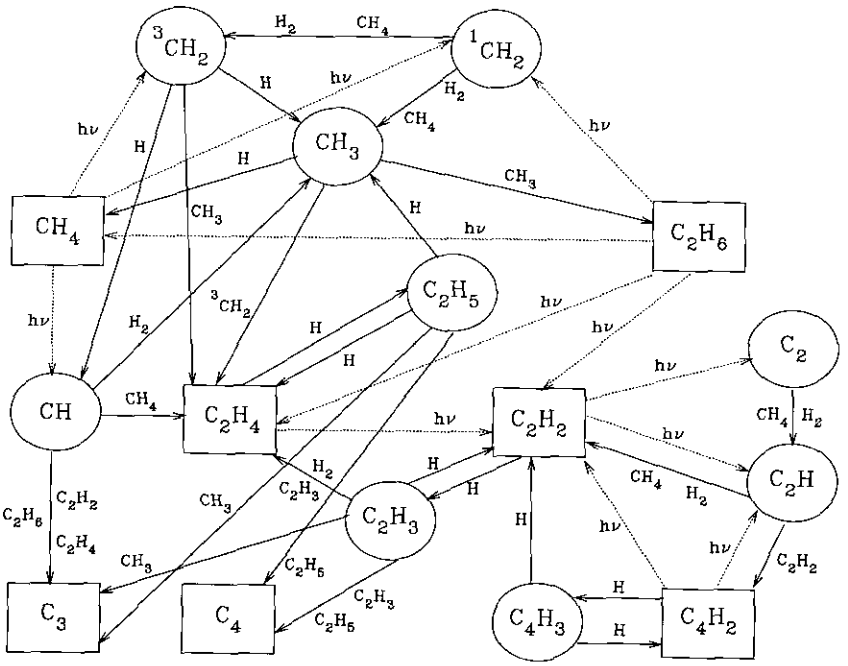

FIG. 2. Diagram of the major photochemical pathways for the reaction scheme in the model. Species in boxes are chemically stable molecules while those in ovals are radicals. Boxes labeled C_3 and C_4 represent more than one C_3 or C_4 species. Solid lines represent chemical reactions while dashed lines are photolysis pathways. See Table II for a complete listing of all of the reactions.

where U_∞ is the fall velocity, and Δz is 1 km. The fall velocities were calculated by

$$U_\infty = \left(1 + \frac{1.26\lambda}{a}\right) U_s, \tag{6}$$

where U_s is the Stokes terminal velocity,

$$U_s = \frac{2a^2 g(\rho_i - \rho_a)}{9\eta_a}, \tag{7}$$

g is the acceleration due to gravity, ρ_i is the mass density of the ice crystal, ρ_a is the mass density of the atmosphere, and η_a is the dynamic viscosity of the atmosphere. The factor multiplying the Stokes velocity in Eq. (6) is the Cunningham correction factor which corrects the Stokes velocity for gas kinetic effects (Pruppacher and Klett 1980). The resultant column densities were converted into number densities by assuming that the aerosols had the same scale height as the background atmosphere in the condensing region.

Thus the condensation loss rate for a given species, L_c, has the functional form

$$L_c = sN_{crys}F, \tag{8}$$

where F is a function that includes the dependence upon crystal radius, shape, vapor pressure, etc. Note that the supersaturation is not constrained to an arbitrary value. For simplicity in our analysis we used different monodispersions in radius for the ice crystals. Recent analysis of PPS data points to a mean radius of 0.2 μm for the stratospheric aerosols on Neptune (Pryor *et al.* 1992) with an upper limit of 0.25 μm. We used radii in the range from 0.1 to 0.5 μm in our analysis. Also, we assumed that each species would only "freeze out" on ice crystals of like composition, e.g., C_2H_2 would freeze out only on C_2H_2 ice crystals. We discuss the validity of, and the sensitivity of the model to, the assumptions used in the condensation loss process in Section IV.

III. MODEL VAPOR PHASE RESULTS: COMPARISON TO IRIS AND UVS OBSERVATIONS

While we compare the model results to the Voyager IRIS and UVS observations, it is important to remember that they are really two different types of measurements. The principal IRIS results are global averages due to the field of view of the individual spectra used and the need to average a large number of spectra to get a sufficient signal to noise (S/N) ratio. The retrieved mixing ratios are also weighted toward the southern hemisphere of Neptune due to the encounter geometry. While there is some latitu-

TABLE III
Summary of Photochemical Model Cases

Case	Model atmosphere	K profile[a]	R63 rate	C_2H_2[b]	C_2H_6[b]
A	Egress nominal	$K \propto N^{-0.6}$, 10^7 at CH_4 homopause	Upper limit	7.2×10^{-8}	6.4×10^{-7}
B	Egress nominal	$K = 2.0 \times 10^3$, $p > 2$ rapid rise, $2 > p > 0.5$ $K = 5.0 \times 10^7$, $0.5 > p > 10^{-3}$ decrease, $10^{-3} > p > 2 \times 10^{-4}$ $K = 5.0 \times 10^6$, $p < 2 \times 10^{-4}$	Upper limit	6.6×10^{-8}	1.5×10^{-6}
C	Egress warm	$K = 2.0 \times 10^3$, $p > 3$ rapid rise, $3 > p > 0.5$ $K = 2.0 \times 10^8$, $0.5 > p > 10^{-3}$ decrease, $10^{-3} > p > 2 \times 10^{-4}$ $K = 5.0 \times 10^6$, $p < 2 \times 10^{-4}$	2.0 × Upper limit	2.4×10^{-8}	8.2×10^{-7}
D	Ingress nominal	$K = 2.0 \times 10^3$, $p > 1.7$ rapid rise, $1.7 > p > 0.5$ $K = 5 \times 10^7$, $0.5 > p > 10^{-3}$ decrease, $10^{-3} > p > 2 \times 10^{-4}$ $K = 5.0 \times 10^6$, $p < 2 \times 10^{-4}$	2.0 × Upper limit	4.9×10^{-8}	1.8×10^{-6}

Note. For all cases the CH_4 mixing ratio at the lower boundary is 10^{-4}, and solar maximum fluxes were used.
[a] p Is the pressure in mbar and K is in units of cm^2 sec^{-1}.
[b] Mixing ratios at 0.5 mbar.

dinal information for acetylene there is none for ethane because of S/N limitations. The IRIS results are sensitive only to ethane and acetylene and in the pressure region 0.1–2.9 mbar for ethane and 0.037–2.3 mbar for acetylene (full width at half maximum of the contribution functions for our egress nominal atmosphere). In contrast, the UVS occultation results are for two specific latitudes, 61°N and 49°S, of which IRIS never saw the former. The UVS lightcurves give information about more hydrocarbons than IRIS: methane and ethylene as well as acetylene and ethane (Bishop *et al.* 1992, Atreya *et al.* 1991a, Yelle *et al.* 1992), but at much lower pressures, e.g., ethane in the 0.02–0.001-mbar region and acetylene in the 0.1–0.005-mbar region. Thus, we have not attempted to satisfy both sets of observations simultaneously; instead we use both data sets to provide modeling constraints. The photochemical model cases are summarized in Table III.

We first constrained the CH_4 mixing ratio at the lower boundary and the strength of K in the upper atmosphere from UVS observations. Bishop *et al.* (1992) showed that the methane mixing ratio must be on the order of 10^{-4} near the lower boundary, and K on the order of 10^7 cm^2 sec^{-1} near 0.2 μbar.

With these UVS constraints on CH_4 and K, we then tried to reproduce the IRIS results. To determine how well a model run matched the IRIS observations the procedure was as follows. Model output (C_2H_2 and C_2H_6 mole fractions vs temperature–pressure levels) were used to generate synthetic spectra. The synthetic spectra were then compared to the observed. If the model calculated mixing ratios did not reproduce the observed emission of both molecules to within the noise uncertainties (±15% for acetylene, ±30% for ethane, both for a given thermal profile), we calculated by how much the model-derived mixing ratios would have to be multiplied to reproduce the observations. This became the "goodness-of-fit" factor for a given set of input parameters and is given in Table IV. Note that this procedure just shifts the model mixing ratio profile; it does not modify its shape. Since height information cannot be extracted from the spectra, the use of a more sophisticated fitting procedure is not justified.

Kostiuk *et al.* (1992) did attempt to derive the ethane height profile in the millibar region by comparing coincident groundbased infrared heterodyne observations with the Voyager IRIS spectra. The higher spectral resolution of the infrared heterodyne measurements probes higher in the stratosphere than that of Voyager IRIS. However, the peaks of the contribution functions of the two instruments were separated by at most a scale height (dependent upon the assumed vertical distribution of C_2H_6). Furthermore, there was a large degree of overlap of the contribution functions. Consequently, no height information could be obtained, and as expected the retrieved ethane mole fractions were consistent with each other within experimental uncertainties.

TABLE IV
Comparison of Photochemical Model Results to Iris Observations

Case	Species	Factor[a]
A	C_2H_2	0.37
	C_2H_6	1.54
B	C_2H_2	0.71
	C_2H_6	0.91[b]
C	C_2H_2	0.91[b]
	C_2H_6	1.25[b]
D	C_2H_2	1.2[b]
	C_2H_6	0.9[b]

[a] The photochemical model mixing ratio must be multiplied by this amount for the model to match the IRIS spectra; e.g., the C_2H_2 mixing ratio in Case A is too high and must be multiplied by a factor of 0.37 for it to match the emission feature.
[b] Within error bounds of measurement.

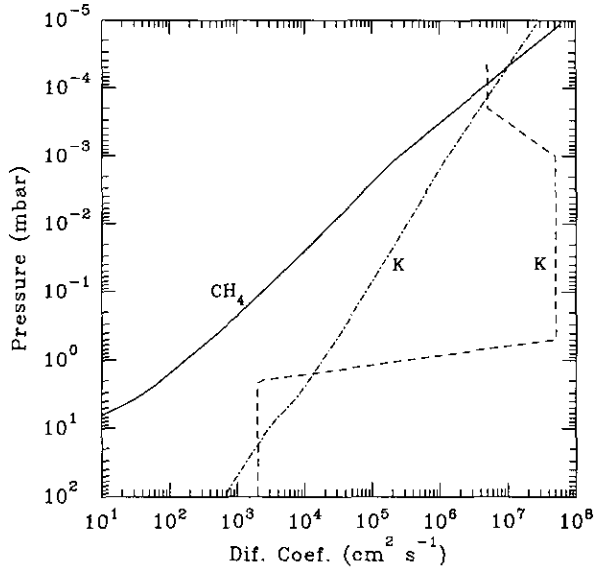

FIG. 4. Eddy diffusion profiles used in the photochemical model to generate the C_2H_6 and C_2H_2 profiles shown in Fig. 3. See Table III and the caption for Fig. 3 for details. Also shown is the CH_4 molecular diffusion coefficient.

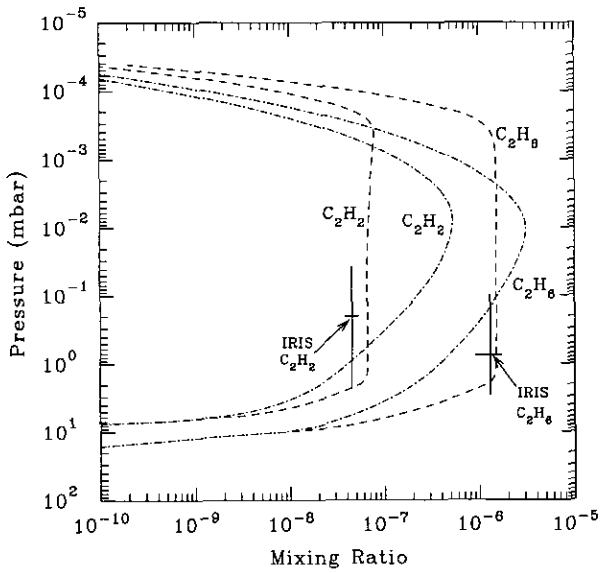

FIG. 3. Photochemical model profiles for C_2H_6 and C_2H_2 for two different K profiles. Dash–dot profiles (Case A) correspond to the dash–dot K profile shown in Fig. 4; similarly, the dashed line profiles (Case B) correspond to the dashed line K profile. Vertical solid lines show IRIS retrieved values of C_2H_6 (1.3×10^{-6}) and C_2H_2 (4.5×10^{-8}) and region of IRIS sensitivity for this model atmosphere (full width at half maximum of the contribution function). Horizontal solid lines show the noise uncertainty in the IRIS-retrieved mixing ratios and are located at the peak of the contribution function. Contribution function calculations were done assuming a constant with height mixing ratio above the condensation region, i.e., similar to the Case B profiles. The CH_4 mixing ratio at the lower boundary is 10^{-4}. The egress nominal thermal profile was used in both the model and data analysis. See Tables III and IV for more information.

In Fig. 3 we present model generated acetylene and ethane mixing ratios for Case A (dash–dot lines) with the corresponding eddy diffusion coefficient shown in Fig. 4 (also dash–dot line). In Fig. 5 and Table IV we compare this case to the IRIS observations. The eddy diffusion coefficient in Case A has the form

$$K \propto N^{-\beta}, \tag{9}$$

i.e., K inversely proportional to the atmospheric number density to some power. For this case $\beta = 0.6$ and K is equal to 10^7 cm^2 sec^{-1} at the CH_4 homopause. This type of K profile has been used in other studies for Neptune (Romani and Atreya 1988 and 1989, Moses 1991). If $\beta = 0.5$ it is representative of transient, but stable, vertically propagating waves (see Hunten 1975, Lindzen 1971). As can be seen in Table IV and Fig. 5, it provides a poor fit to the IRIS C_2H_2 and C_2H_6 data. In comparison with the IRIS data the model C_2H_2 is 2.7 times too high, while the C_2H_6 is 1.5 times too low. This case is typical of a "best fit" to the IRIS data using this type of K profile: too much C_2H_2 relative to C_2H_6. As in Bézard *et al.* (1991) we find that it is possible to reproduce either the observed acetylene or ethane emission to within the noise uncertainties with this form of K. However, the fit to the other species then becomes worse than in Case A. Changing the CH_4 mixing ratio at the lower boundary, the homopause value of K, or the value of β within the limits of the UVS data produced no better results.

In Fig. 6 we show UV lightcurves generated with Case

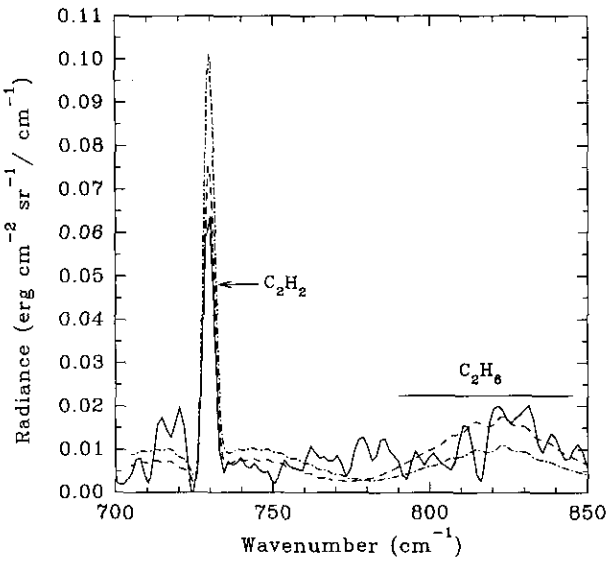

FIG. 5. Comparison of the IRIS global-average spectrum (solid line) to synthetic spectra generated using Case A (dash–dot line) and Case B (dashed line) C_2H_2 and C_2H_6 mole fraction profiles. Case B clearly provides a better fit to the data.

A in comparison with the UVS egress occultation data, using the techniques described in Bishop *et al.* (1992). It is obvious that this case, which is geared primarily toward replicating the IRIS data, fails to provide an acceptable fit to the UVS data: CH_4 mixing ratios near 0.2 μbar are too small by a factor of ~60 to reproduce the correct half-light altitudes at wavelengths <140 nm, and C_2H_2 mixing ratios are too large by a factor ~10^2 (as evidenced by the lightcurves at 152 nm). There is also a problem at wavelengths >153nm where C_2H_4 is the major source of opacity. Alternately, cases can be constructed with the goal of replicating solely the UVS occultation data using an eddy mixing profile given by Eq. (9). Attempts along these lines have been described by Atreya *et al.* (1991a). It is possible to get an acceptable fit to the UVS data at wavelengths <140 nm (methane dominated) using a K profile given by Eq. (9) with $\beta = 0.6$, a methane mixing ratio in the lower stratosphere of 10^{-4}, and a CH_4 homopause value of K of ~5×10^8 cm^2 sec^{-1}. However, the problems with too much UV opacity from C_2H_2 and C_2H_4 and too little IR emission of C_2H_6 in comparison to C_2H_2 remain.

We then tried different types of K profiles. In Fig. 3 we show Case B C_2H_2 and C_2H_6 mixing ratios (dashed lines) which provide good agreement with the IRIS observations and a considerably better fit to the UVS egress data (see Table IV and Figs. 5 and 6). Case B C_2H_6 abundances are within the measurement uncertainties of the IRIS value while the acetylene abundance is only 30% too high; as regards the UVS data, the fit fails to be acceptable only at wavelengths >150 nm, where there is too much opacity from acetylene and ethylene. The corresponding K profile is shown in Fig. 4 (dashed line). At pressures greater than 2 mbar K is constant at 2×10^3 cm^2 sec^{-1}. This value is based upon the circulation pattern in the lower stratosphere derived in Conrath *et al.* (1991). The overturning time constant associated with the residual mean circulation, the circulation that results in mixing, is on the order of 10^9 sec (Conrath, personal communication, 1993). We equated this to the eddy time constant, H^2/K, to derive the value of the eddy diffusion coefficient. Between 2 and 0.5 mbar, K rapidly rises to a new constant value, 5×10^7 cm^2 sec^{-1}. This rapid increase in K has the effect of separating the condensation loss region for C_2H_2 and C_2H_6 from the region where most of the photochemistry (production) transpires, giving rise to the change in slope of the mixing ratio profiles at about 2 mbar. A rapid change in K could be caused by wave dissipation in this region and there is some indication of this in the RSS data (Hinson and Magalhães 1993). Finally, K decreases in the pressure region 10^{-3} to 2×10^{-4} mbar and is taken to be constant at smaller pressures. A decrease in K near 1 μbar is suggested by photochemical modeling of the UVS lightcurves (Atreya *et al.* 1991a), but the precise form for the K profile cannot be uniquely determined from the UVS data. Briefly, if such a decrease were not present, then the abundances of the stable C_2 hydrocarbon species tend to be too large to be consistent with the UVS data. This is especially true for ethylene: most C_2H_4 production (mainly via R4) occurs at higher altitudes than the main chemical loss channel (R63), so that a decrease in K with decreasing pressure in this region biases the transport of ethylene downward, resulting in lower overall abundances.

The presence of a decrease in K as the homopause is approached is not in itself surprising. Lindzen (1981) presented a parameterization of K that addresses the "breaking" of upwardly propagating waves in the terrestrial mesosphere; in particular, K increases rapidly in the vicinity of the breaking level. Lindzen was mainly concerned with parameterizing the wave drag acceleration of the mean zonal flow, and his parameterization exhibits a strong dependence on the difference between the mean zonal wind speed and the wave zonal phase speed. This leads to a marked decrease in K at smaller pressures for mid-latitudes, where the deposition of momentum by breaking waves strongly affects upper mesospheric wind speeds. Even at low latitudes, Lindzen argued for a decrease in K at altitudes above the breaking level for tides (and below the nominal homopause), since the rapid increase in molecular diffusion as the homopause is approached will itself act to damp the tide so that less mechanical mixing is needed. Holton and Schoeberl (1988) have argued that the Lindzen parameterization is inappro-

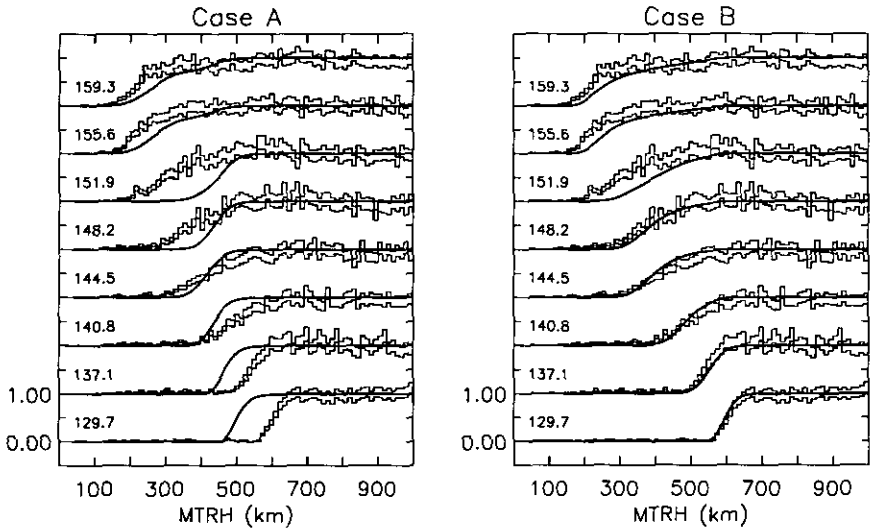

FIG. 6. (Left) Comparison of UVS egress solar occultation lightcurves (130–160 nm) acquired at Neptune (Broadfoot *et al.* 1989) with lightcurves calculated using the mixing ratio profiles shown in Fig. 3 for Case A. The model lightcurves include opacity from methane, ethylene, acetylene, ethane, and H_2 Rayleigh scattering as discussed in Bishop *et al.* (1992) and Atreya *et al.* (1991a). The UVS data, obtained at 49°S latitude, are displayed as lightcurve pairs: $I(z)/I_0 \pm \sigma_D$, where σ_D denotes the measurement uncertainty that varies with minimum tangent ray height. This model is clearly not consistent with the UVS data; this is most obvious in the lack of opacity at wavelengths <140 nm where methane is the dominant absorber and the strong C_2H_2 absorption in the model at 152 nm. (Right) The UVS egress solar occultation data are here compared with model lightcurves for Case B. This model provides a far better fit to the UVS data; the lack of agreement is mainly confined to wavelengths >150 nm, where the abundances of acetylene and ethylene are apparently too large to be consistent with the measured opacities.

priate for constituent transport and that the vertical transport of a minor species is more likely due to advection within a meridional circulation system (unless the species in question is characterized by relatively short photochemical time scales). Notably, the effective one-dimensional vertical transport coefficient they propose, defined in terms of an area-weighted global average of vertical wind speeds derived from simple numerical simulations, also exhibits a decrease at altitudes above the level where maximum meridional wind speeds occur. What is most significant in the context of one-dimensional photochemical models is that the decrease in K exhibited in either scenario occurs at altitudes beneath the nominal homopause (the level above which molecular diffusion is the main process governing vertical transport). Thus, while it remains to test the suggestion that K does decrease as the homopause is approached against reliable dynamical models of outer planet stratospheres, terrestrial analogs indicate that such a decrease is at least plausible.

Of the numerous K profiles that we explored, only those having a rapid rise in the mbar region led to improved model agreement with both the IRIS and UVS data. This type of K profile works well because it satisfies the seemingly contradictory requirements on K in the lower stratosphere. The IRIS C_2H_6 observations require weak eddy diffusion, but the IRIS C_2H_2 observations, and UVS constraints on C_2H_2 and C_2H_4, require vigorous eddy diffusion.

Low eddy diffusion near 0.5 mbar improves the model fit to the IRIS ethane observations because of the derived high mixing ratio and its chemical stability in the region sounded by IRIS. Kostiuk *et al.* (1992) showed that the peak of the ethane contribution function occurs between 0.2 and 0.7 mbar for a wide variety of ethane mixing ratio profiles. The source of the ethane is at much lower pressures (microbar region) and there is not a significant chemical sink for ethane in the 0.1 to 1.0 mbar region. In the region sounded by IRIS ethane is then flowing from a source at lower pressures to a condensation sink at higher pressures. Under these conditions the downward flux must balance the column chemical production or

$$fNv = P_{chem}, \tag{10}$$

where f is the ethane mixing ratio, v is the downward transport velocity to the condensation region, and P_{chem} is the column chemical production rate of ethane. We can determine the maximum value of v compatible with the ethane data by using the maximum value of P_{chem}. The maximum production occurs if all the photons that methane can absorb convert it to ethane with 100% efficiency. For global average conditions this results in a maximum ethane production of 2.7×10^8 molecules cm^{-2} sec^{-1}. Applying the above equation at 0.5 mbar leads to an upper limit to the transport velocity of 7×10^{-3} cm sec^{-1}. Using

$K = v\,H$ as a first-order estimate to v we obtain an upper limit to K of $\approx 3.0 \times 10^4$ cm^2 sec^{-1} at 0.5 mbar.

However, best fits to the C_2H_2 observations and upper limits to C_2H_4 require faster transport rates (larger K values) than this. Vigorous eddy diffusion in the lower stratosphere improves the model fits to the IRIS C_2H_2 emission and the UVS constraints on C_2H_2 and C_2H_4 because of their derived low mixing ratios and the placement of their chemical sources and sinks. Acetylene and ethylene are similar in that they are produced primarily at low pressures and have strong losses via three-body hydrogen addition reactions (R63 for C_2H_4 and R62 and C_2H_2) which are most efficient at higher pressures. Rapid downward transport of H along with C_2H_2 and C_2H_4 reduces the mixing ratios of these two hydrocarbons. There are additional complications with acetylene, though. The product of R62 is vinyl which often recycles acetylene via R37. However, in our model a significant fraction of C_2H_3 undergoes a three-body reaction with CH_3 to form C_3H_6 (R22). If we turn off R22 the acetylene mixing ratio in Case B doubles. (Our rates for R22 are $k_0 = 1.3 \times 10^{-22}$, and $k_\infty = 1.2 \times 10^{-10}$ Laufer *et al.* 1983, Fahr *et al.* 1991.) Acetylene also has an important low altitude source from C_2H_4 photolysis (J3A and J3B) occurring just above the condensation region.

The Case B eddy profile improves the model fit to the observations in the following way. The high value of K for pressures less than 0.5 mbar results in rapid transport of C_2H_2 and C_2H_4 to their chemical sink regions and reduction of their mixing ratios. (The high value also transports CH_4 to low pressures as required by the UVS occultations.) However, the rapid decrease in eddy diffusion at pressures greater than 0.5 mbar produces a bottleneck in downward transport that results in an increase in the ethane mixing ratio. Because of the rapid decrease in K the transport velocity in Case B at the 0.5 mbar is $\approx K_S/H$, where K_S is the value of K in the stagnant region, 2.0×10^3 cm^2 sec^{-1}, not the K at the 0.5 mbar level ($\approx 10^5$ cm^2 sec^{-1}). We then explored the sensitivity of the model results with this type of K profile to the chemistry, the level where the rapid increase in K begins, and the thermal profile.

With respect to the reaction rates, the C_2H_6 and C_2H_2 mixing ratios predicted by the model are very sensitive to the value of the rate constant for reaction R63,

$$C_2H_4 + H + M \rightarrow C_2H_5 + M \qquad \text{R63},$$

especially the low-pressure rate constant. We are currently using the upper limits to this rate constant as given in Lightfoot and Pilling (1987),

$$k_0 = 2.15 \times 10^{-29}\, e^{(-349/T)}$$

$$k_\infty = 4.95 \times 10^{-11}\, e^{(-1051/T)} \qquad (11)$$

$$k = \frac{k_0 k_\infty M}{k_0 M + k_\infty},$$

where k_0 is the limiting low-pressure rate constant, k_∞ is the high-pressure limit, k the overall rate, and M the atmospheric number density. If instead we had used the nominal value of k_0 in Lightfoot and Pilling (1987),

$$k_0 = 1.39 \times 10^{-29}\, e^{(-569/T)}, \qquad (12)$$

the C_2H_2 mixing ratio in Case B increases from 6.6×10^{-8} to 1.7×10^{-7} while C_2H_6 decreases from 1.5×10^{-6} to 1.1×10^{-6} (all mixing ratios pertain to the 0.5-mbar region). Using nominal values for both k_0 and k_∞ produce no further change in the acetylene and ethane mixing ratios in Case B.

The reason why these changes occur is that destruction of ethylene by R63 leads to ethane production via

$$C_2H_4 + H + M \rightarrow C_2H_5 + M \qquad \text{R63}$$

$$C_2H_5 + H \rightarrow 2\,CH_3 \qquad \text{R46}$$

$$CH_3 + CH_3 + M \rightarrow C_2H_6 + M \qquad \text{R21}.$$

The other major sink for C_2H_4 is photolysis to C_2H_2:

$$C_2H_4 + h\nu \rightarrow C_2H_2 + H_2 \qquad \text{J3A}$$

$$\rightarrow C_2H_2 + 2\,H \qquad \text{J3B}.$$

Thus, increasing the rate constant for R63 increases the fraction of C_2H_4 converted to C_2H_6 while decreasing the fraction converted to C_2H_2. Also, increasing the rate of R63 rate helps in reproducing the UVS lightcurves by reducing the ethylene mixing ratio. With the nominal rate there is too much C_2H_4 in the model compared to the UVS data.

It is not unreasonable to use the upper limit to k_0. The lowest temperature that Lightfoot and Pilling (1987) went to was 285 K while we need the rate at temperatures at least 100 K lower. Their value of k_∞ was derived by using their data in the range of 285 to 604 K and low-temperature data of Lee *et al.* (1978) from 198 to 320 K. Lee *et al.* (1978) derived an energy barrier of -1040 K close to the fast k_∞ value of Lightfoot and Pilling (1987). So it may not be unreasonable to expect a lower energy barrier for k_0 at lower temperatures as well. Of course, what is really needed is a good laboratory measurement of this reaction rate at low temperatures in the fall-off regime.

With respect to the K profile, the acetylene and ethane mixing ratios in the region sounded by IRIS are most sensitive to the pressure, p_0, where the rapid increase in

TABLE V
Ethane and Acetylene Sensitivity to K Profile

Pressure (mbar)[a]	C_2H_2[b]	C_2H_6[b]
5	2.9×10^{-8}	3.7×10^{-7}
2	6.6×10^{-8}	1.5×10^{-6}
1	8.2×10^{-8}	2.7×10^{-6}

[a] At pressures greater than this value K is constant at 2.0×10^3 cm^2 sec^{-1}, at lower pressures K begins to increase rapidly with height. All other parameters are the same as in Case B given in Table III.

[b] Mixing ratios at 0.5 mbar.

K begins. In Table V we show model results with p_0 of 5, 2, and 1 mbar. (Note that 2 mbar is the Case B value.) The trend is for decresing mixing ratios for increasing values of p_0. For ethane this is easily understood. As discussed above, ethane is being transported downward from a production region to a loss region with transport limited by the low value of K in the stagnant region. We can then solve approximately for its mixing ratio, f, immediately above the stagnant region by rewriting Eq. (10) as

$$f \approx \frac{P_{\text{chem}} H}{N_0 K_s}, \tag{13}$$

where N_0 is the number density at p_0. The ethane mixing ratio then changes due to the change in N_0—increasing the pressure increases N_0 and thus f decreases. For acetylene it is slightly more complicated. It shows the same trend as ethane but to a smaller degree. The reason is that, as mentioned previously, acetylene is produced locally in this region. Increasing the pressure increases the extent of the production region. Thus the effect of increasing N_0 in Eq. (13) is offset by increased production.

Lastly, we examined the sensitivity of these results to the thermal profile. We compared ingress and egress cases primarily for possible effects on haze composition (see Section II.A). In addition to this comparison, we also examined the impact of a warm model atmosphere. This is because the groundbased observations of methane emission can be reproduced better with the methane mixing ratio adopted here (10^{-4}) if the warm model atmosphere is used (Orton *et al.* 1992). Also, the UVS data are better fit with a lower C_2H_2 abundance than the IRIS data for the nominal atmosphere, which suggests a warmer atmosphere. The use of a colder model atmosphere would exacerbate the discrepancy in the data sets, and thus it was not used. We also at this time increased the rate constant for R63 above its upper limit to see if we could improve the fit to the data. We did so simply, by multiplying the high and low pressure rate constants by 2, rather than try combinations of the preexponential factor and the energy barrier for both k_∞ and k_0.

In Fig. 7, we show model acetylene and ethane mixing ratios for the warm egress atmosphere (Case C) and in Figs. 8 and 9 we compare this case to the IRIS and UVS observations, respectively. Note that the warm model atmosphere was used in both the photochemical model and in the analysis of the IRIS and UVS data for self-consistency. With the warm model atmosphere the retrieved acetylene and ethane mixing ratios from the IRIS observations decrease due to the well-known temperature/abundance interdependence for infrared emission modeling. The retrieved C_2H_2 abundance is more sensitive to this than the C_2H_6 with its mixing ratio decreasing by a factor of 2, while the ethane decreases by only 1.3. So, in contrast to the nominal model atmosphere cases, the photochemical model must produce both lower mixing ratios and a larger $[C_2H_6]/[C_2H_2]$ ratio. Comparing Case B to C in Table III shows how this was accomplished. Increasing the pressure where K begins to rapidly increase from 2 to 3 mbar, reduces both mixing ratios. Increasing K in the well mixed region by a factor of 4 enhances C_2H_2 loss. Lastly, increasing the R63 rate increases $[C_2H_6]/[C_2H_2]$. As can be seen in Table IV both the model-predicted C_2H_2 and the C_2H_2 mixing ratios for Case C are within the IRIS measurement uncertainties. Additionally,

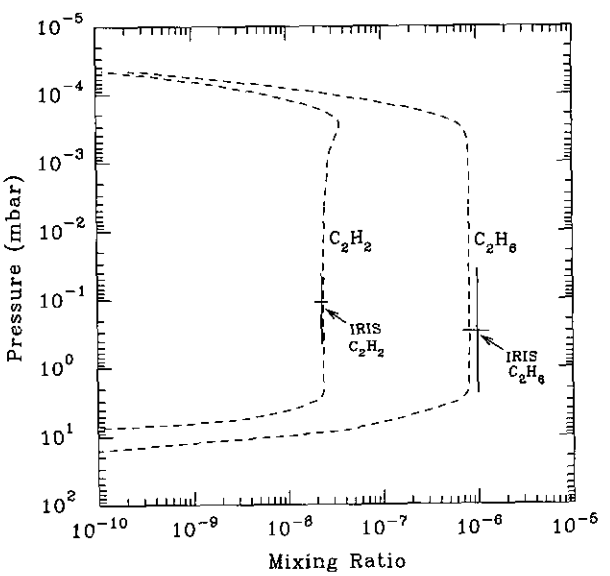

FIG. 7. Photochemical model profiles (dashed lines) for C_2H_6 and C_2H_2 for the egress warm thermal profile (Case C). The IRIS-retrieved values of C_2H_6 (1.0×10^{-6}) and C_2H_2 (2.3×10^{-8}), the region of IRIS sensitivity for this model atmosphere, and the noise uncertainty in the IRIS-retrieved mixing ratios are shown as in Fig. 3. The CH_4 mixing ratio at the lower boundary is 10^{-4}.

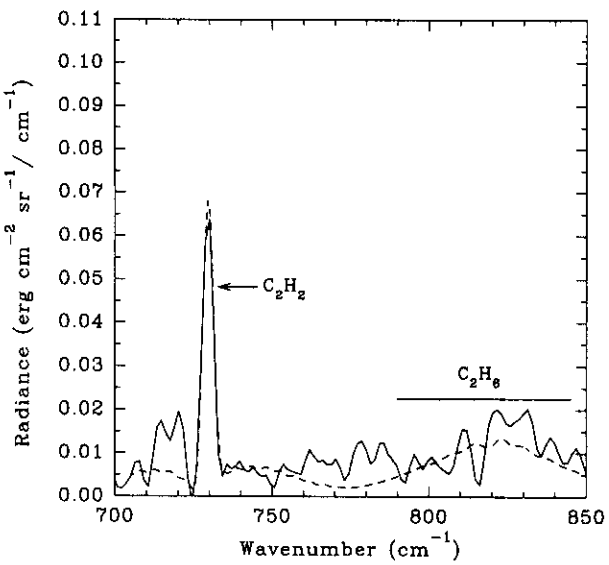

FIG. 8. Comparison of the IRIS global-average spectrum (solid line) to the synthetic spectrum generated using Case C hydrocarbon mole fractions (dashed line). The egress warm model atmosphere was used in generating the synthetic spectrum.

the latter two changes also yield model ethylene mixing ratios consistent with the UVS lightcurves.

The C_2H_2 and C_2H_6 profiles for the nominal ingress model atmosphere case, Case D, are so similar, both qualitatively and quantitatively, to the Case B profiles that for brevity we do not show them. We do summarize the differences between the cases in Table III and give the goodness-of-fit factors in Table IV. The major difference is that use of the faster R63 rate in Case D results in both C_2H_2 and C_2H_6 from the model matching the IRIS observations.

The major caveat in deducing the eddy profile from the C_2H_2 and C_2H_6 observations is that it is dependent upon knowing the photochemistry adequately. To illustrate this, we note that Bézard *et al.* (1991) tried K profiles similar to those used in Cases B, C, and D but did not see an improvement in model fits to the data. Thus, photochemical modeling should be viewed as an evolving process: using what is currently known about the photochemistry, *K* profiles are deduced from model-observation comparison and key reaction rates and consequences of the *K* profile are identified. We have investigated ways in which unknowns in the chemistry could affect our conclusions. Seeing the sensitivity of the model results in Case B to the rate for R63 we doubled this rate with the Case A *K* profile. This did not improve the model fit. We note that Moses (1991), using a photochemical reaction scheme that includes more C_3 and C_4 hydrocarbon photochemistry than ours, was also not able to match simultaneously the IRIS acetylene and ethane with Eq. (9)-type *K* profiles. The problem was the same as the problem we observed: too much C_2H_2 relative to C_2H_6. There is also reasonable agreement between the two models given similar inputs (see above).

Recently, Mordaunt *et al.* (1993) have determined that CH_3 is produced with a quantum yield of $\approx$0.5 in methane photolysis at Lyman α. At first glance this would seem to be a major perturbation to the chemistry. With respect to the production of CH_3, however, it is not a major change. In the model $^1CH_2$ is produced at Lyman α with a quantum efficiency of 0.41 and the $^1CH_2$ rapidly reacts with H_2 to form CH_3. Thus the model already has, via a two-step process, the production of CH_3 from CH_4 photolysis

$$\begin{array}{lr} CH_4 + h\nu \rightarrow {}^1CH_2 + H_2 & J1B \\ {}^1CH_2 + H_2 \rightarrow CH_3 + H & R9 \\ \hline CH_4 + h\nu \rightarrow CH_3 + H & Net \end{array}$$

at approximately the right quantum yield. What is important, and was not well determined by Mordaunt *et al.* (1993), is the production of CH and $^3CH_2$ vs CH_3 and $^1CH_2$. As seen above, $^1CH_2$ leads to CH_3 and consequently C_2H_6 production. $^3CH_2$ is primarily lost to CH (R14) and

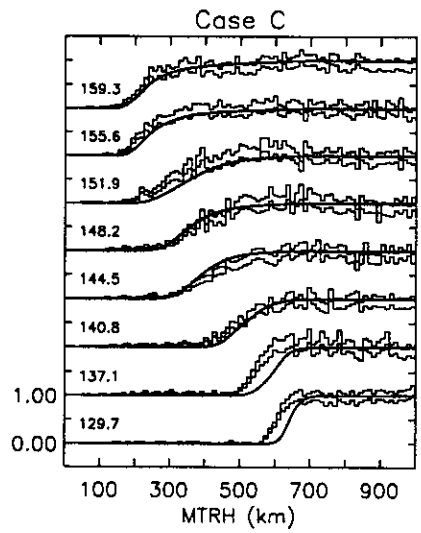

FIG. 9. The UVS egress solar occultation data (Broadfoot *et al.* 1989, and Atreya *et al.* 1991a) are compared with Case C model lightcurves. This model, with its warmer temperatures at pressures <0.1 mbar, exhibits too much CH_4 opacity; recall that the mixing ratio of methane in the lower stratosphere has been fixed at 10^{-4} in all of the models (see text) and the *K* profile has not been constructed with the specific goal of satisfying the UVS data. The fit to the UVS data at wavelengths >140 nm is nonetheless fairly good. If the CH_4 mixing ratio had been reduced to fit the UVS methane-dominated channels, the IRIS C_2H_2 and C_2H_6 emission features would still be reproduced by the model to within the IRIS noise uncertainties.

CH leads to C_2H_4 (R4) and subsequently C_2H_2 production (J3A and J3B). If the result of further experiments shows that the present model has a too-high/low production of CH and $^3CH_2$ vs $^1CH_2$ and CH_3 then the model has a too-high/low production rate of C_2H_2 to C_2H_6. If it is shown that we currently overestimate the production of C_2H_2 and C_2H_4 then our conclusion about the need for a fast rate constant for R63 will be altered and perhaps the nominal value for this rate will allow the model to match the data. Also, since R22 is an important sink for C_2H_2, improved laboratory measurements of its reaction rate as a function of pressure and temperature are important.

There are observational tests of our prediction for the K profile. The height profiles of acetylene and ethane in the millibar region are quite different from Case A to Case B, so measurements of the vertical profiles of these hydrocarbons in this region would be useful. As noted in Kostiuk *et al.* (1992), if the goundbased heterodyne data had higher signal-to-noise retrieval of height information would have been possible. It is also worth noting that, while the strength of K in the vigorously mixed region ($p < 0.5$ mbar) exceeds the value predicted by Hinson and Magalhães (1993) by roughly two orders of magnitude, the placement of the pressure level at which a rapid rise in K is required in our models is in line with their study. Hinson and Magalhães themselves note that the Lindzen parameterization they adopted yields only a rough approximation to the magnitude of K at best. Also, the RSS data refers to only two specific latitudes. In contrast, K derived from 1-D photochemical modeling necesarily includes the effects of global and mesoscale dynamics in addition to localized mixing process. The IRIS data used in the modeling is a global average. Given these caveats, it is hard to attribute much meaning to the apparent discrepancy in the magnitude of K near 0.1 mbar from the RSS and IRIS data.

IV. MODEL HAZE RESULTS AND COMPARISON TO OBSERVATIONS AND OTHER MODELS

IV.A. Results

In Table VI we present results of haze calculations for the cases which have good vapor phase agreement with the IRIS and UVS observations: B, C, and D. For acetylene and ethane (the only species for which we have firm constraints on the vapor phase abundance near the condensation region) we show the levels where the hazes first form, the column mass production rates (g cm^{-2} sec^{-1}), and the haze particle column number densities (particles cm^{-2}) as a function of the assumed haze particle radius. The column densities were calculated as described in Section II.E. The condensation temperature of each species is essentially constant across the three cases for reasons given in Section II.A. Between Cases B and D, however, the pressure of the condensation level increases, because the ingress model atmosphere (Case D) is warmer than the egress model atmosphere (Case B) in the region where the hydrocarbons condense (see Fig. 1).

TABLE VI
Summary of Model Haze Results

Species		Case B	Case C	Case D
C_2H_2				
	Level[a]	6.9 mbar, 73 K	6.9 mbar, 73 K	9 mbar, 73 K
	Prod[b]	3.4×10^{-16}	2.8×10^{-16}	2.9×10^{-16}
	0.1 μm	1.1×10^{8}	9.1×10^{7}	1.4×10^{8}
Col den[c]	0.2 μm	6.2×10^{6}	5.3×10^{6}	8.2×10^{6}
	0.5 μm	1.3×10^{5}	1.1×10^{5}	1.6×10^{5}
C_2H_6				
	Level[a]	10 mbar, 64 K	10 mbar, 64 K	16 mbar, 63 K
	Prod[b]	7.2×10^{-15}	7.4×10^{-15}	7.5×10^{-15}
	0.1 μm	2.4×10^{9}	2.5×10^{9}	3.9×10^{9}
Col den[c]	0.2 μm	1.4×10^{8}	1.5×10^{8}	2.2×10^{8}
	0.5 μm	3.0×10^{6}	3.1×10^{6}	4.3×10^{6}
C_3H_6[d]				
	Level[a]	6.9 mbar, 73 K	8.2 mbar, 68 K	11 mbar, 69 K
	Prod[b]	1.6×10^{-15}	9.5×10^{-16}	1.2×10^{-15}
C_3H_8[d]				
	Level[a]	6.9 mbar, 73 K	6.9 mbar, 73 K	9.0 mbar, 73 K
	Prod[b]	9.6×10^{-16}	1.0×10^{-15}	1.2×10^{-15}
Total prod[b]		1.1×10^{-14}	9.6×10^{-15}	1.0×10^{-14}

[a] Pressure and temperature where species first begins to condense.
[b] Haze production rate in g cm^{-2} sec^{-1}.
[c] Column density of hazes in particles cm^{-2} as a function of particle radius.
[d] Calculations are approximate; see text for details.

Ethane is clearly the dominant haze component with its production accounting for ≈75% of the total haze mass production rate. The next most abundant components are C_3H_6 and C_3H_8 which together account for approximately 22% of the total mass production rate (see discussion below, however). The smallest component is C_2H_2, its mass production rate is only about 3% of the total. There is less than a factor of two variation in the haze production rate across the three cases for all the species. The net chemical production rates of these species have little variation in them and these rates control the haze production in our steady-state model (see Section II.E). The changes in the vapor phase mixing ratios among the cases are caused more by changes in the K profile (see Table III) than by changes in the net chemical production rate.

We do not include C_4H_2 in Table VI because its haze production rate never amounted to more than 0.25% of the total mass production rate. This is different from Uranus, where it has been predicted to be a significant component of the haze (Atreya *et al.* 1991b, Summers and Strobel 1989). The diacetylene haze is unlike the acetylene and ethane hazes with 90% or more of its production occurring *in situ*, i.e., in the region where it is cold enough that C_4H_2 condenses immediately upon vapor phase production. In contrast, 100% of the ethane haze and 93% or greater of the acetylene haze is the result of downward transport of these molecules. Consequently, the C_4H_2 mass production rate showed the most variation among the three cases.

For Case B the mass production rate was 6.3×10^{-18} g cm^{-2} sec^{-1} while for Case D it was 1.4×10^{-17} g cm^{-2} sec^{-1}. The reason for this doubling is that there is a larger region of C_4H_2 haze formation in the ingress model atmosphere.

The condensation levels and mass production rates of C_3H_6 and C_3H_8 are only approximate. As mentioned in Section II, a significant fraction of the carbon atoms lost by methane due to photochemical destruction produce C_3 and C_4 hydrocarbons. We show haze calculations for these two C_3 species because of their large mass production rates and they are not free radicals. We took the chemical production rate profiles for propene and propane and solved for their mixing ratio profiles, assuming only transport and condensation, i.e., no further chemistry. Their vapor pressures were calculated by curve-fitting to data given in Ziegler (1959). The estimated mixing ratios for both of these species is about 6.8×10^{-8}. To check these simple calculations we compared the predicted C_3H_6 and C_3H_8 mixing ratios with the IRIS and UVS observations using the same method we used for C_2H_2 and C_2H_6. The C_3H_8 abundance is below the IRIS detectability limit and lack of IR spectral information prevents us from checking the C_3H_6 mixing ratio. Preliminary UVS comparisons, however, indicate that these C_3H_6 and C_3H_8 mixing ratios are too large. This probably indicates that these compounds undergo subsequent photochemistry. We realize that these calculations are only approximate and show them as illustrative examples of the potential source of the C_3 and C_4 species to the stratospheric haze in our model.

The haze production rates of acetylene and ethane are independent of the particle radius in the range we investigated. This is not necesarily so. The condensation loss process is dependent upon particle radius (see Eqs. (2) and (3)) and particle number density (Eq. (8)) which is in turn dependent upon the crystal radius through the sedimentation velocity. The haze column production rate would change if the condensation time became so long that eddy transport could effectively compete with it. In this case the aerosol flux *and* vapor phase transport of a species through the lower boundary would balance the net column chemical production rate. This would be a consistent scenario but our assumption used in calculating N_{crys}, that the aerosol production rate alone must balance the net chemical production rate, would have been incorrect. However, for all of the crystal radii considered here, condensation loss was much faster than eddy transport.

A measure of the effectiveness of condensation loss for a species is its supersaturation (see Eq. (8)). If the product of the number density of crystals and the diffusion loss rate is low the supersaturation must be large for condensation loss to be important. For acetylene and ethane condensation loss is very effective with supersaturations of 10^{-2} or less for the range in particle radius we investigated. The largest supersaturations, and most of the haze production, for these two species occurs in the first few levels where condensation begins. However, significant supersaturations (>1000) do build up for diacetylene. Its chemical production is balanced by condensation loss at each level (both eddy transport and chemical loss are much slower than condensation loss). The chemical production decreases by only an order of magnitude from low to high pressure in the C_4H_2 condensation region, but the vapor pressure decreases by 15 orders of magnitude. Since condensation loss is directly dependent upon the vapor pressure (Eq. (2)), the supersaturation increases.

To derive a number density profile of the crystals from the constraint on the column density we assumed that the crystals were distributed with the gas scale height. We now examine if this assumption is consistent with our results. In doing so it is important to keep in mind that our calculated haze column densities are the result of a simple flux balance—photochemical production balanced by sedimentation loss. Our arguments then apply to the aerosol particles that are responsible for the sedimentation flux, that is, those particles that have grown to a size such that sedimentation is faster than any growth process. As mentioned above, the ethane and acetylene hazes in our model are produced just below the condensation level. The mass flux of a given species, i.e., the product of the number density of crystals and velocity, is then constant throughout most of the haze region. To determine which velocity profile to use to derive the number density profile we must compare the fall time, τ_{fall}, to the eddy diffusion time, τ_{eddy}. If $\tau_{eddy} < \tau_{fall}$ then the eddy velocity is the correct one. In our models, this occurs only for the 0.1-μm radius particles. As is seen below observations indicate larger particle radii. Therefore, for the range in particle radius of interest $\tau_{fall} < \tau_{teddy}$, and the sedimentation velocity should be used. Since the fall velocity varies roughly as $1/N$, the ice crystal number density must increase with N to preserve the constant flux condition, i.e., the number density of the crystals varies with the atmospheric scale height. However, our predicted haze production rate and column density is independent of the assumed distribution of haze particles.

We place the bottom of the haze at the tropopause for several reasons. As the ice particles fall below the tropopause the temperature increases; thus, the ice particles will eventually sublimate. We recognize that this is an approximation to the true sublimation level. We cannot follow the particles as they sublimate because we do not have a sublimation loss for the crystals in the model. Also, below the tropopause we expect the eddy mixing to increase. The sedimentation velocity is still decreasing due to the increase in atmospheric number density. This will result in the eddy velocity dominating and the velocity

in the flux equation increasing; thus, the number density of the haze particles will decrease.

IV.B. Comparison to Observations

IV.B.1. Voyager PPS. Pryor *et al.* (1992) from analysis of Voyager PPS observations at 2650 and 7500 Å deduced a stratospheric aerosol column density of 2.5–6.2 $\times$ 10^7 cm^{-2}. The majority of this haze is at pressures greater than 15 mbar with only 10% of the burden in the 5–15-mbar region. The 2650-Å observations imply a mean particle radius of 0.2 μm, while the 7500 Å favor slightly larger particles—0.25 μm. As the 2650 Å data probe lower pressures than the 7500 Å data, this is suggestive that the particles grow in radius as they settle out of the stratosphere. The most recent analysis of groundbased observations of Neptune's stratospheric aerosols is in fairly good agreement with the PPS data. For 0.2-μm-radius particles Baines and Hammel (1992) derived a column density of 6.4 $\times$ 10^7 cm^{-2} for global average conditions.

Our predicted altitude location of the haze agrees with the PPS-derived location. The hydrocarbons condense only at pressures greater than 5 mbar, and ethane, the dominant source of the haze, does not condense out until 10–16 mbar. However for 0.2-μm-radius particles our computed haze burden is too large—1.94 $\times$ 10^8 particles cm^{-2}. If we use the upper limit in particle radius, 0.25 μm, we get better agreement. Our predicted haze column density drops to 7.7 $\times$ 10^7, only 24% too high. However, there are two possible reasons why this simple calculation overpredicts the haze production from the model.

The above haze column densities were calculated assuming that C_3H_6 and C_3H_8 condense. If instead we assume that they are converted to other hydrocarbon species that do not condense then the model-predicted haze density decreases. Neglecting the propane and propene contribution the haze column density for 0.25-μm-radius particles becomes 5.8 $\times$ 10^6 particles cm^{-2}, below the PPS upper limit. Some justification for this comes from our preliminary calculations that showed too much UV opacity in the model compared to the UVS occultation lightcurves when we included C_3H_6 and C_3H_8 calculated assuming no chemical loss. This, by itself, suggests that these compounds are converted to other species. However, what fraction of the propane and propene are converted into noncondensing species can be answered only with further modeling of the C_3 photochemistry.

The other problem with the above calculation is that it was done with solar maximum fluxes. We have shown that the acetylene and ethane components of the haze are the result of downward transport. In the haze formation region the eddy transport time is longer than a solar cycle as is the sedimentation time for 0.2- to 0.25-μm radius spheres. So the observed haze density is the result of solar fluxes averaged over a solar cycle. We ran the photochemical model with the same input parameters as Case B but for solar minimum conditions. Note that this also reduces the LISM Lyman α because it is predominantly due to scattering of the solar Lyman α line. Under these conditions the model haze column density, including the propane and propene contribution, is below the PPS upper limit for 0.22-μm-radius particles.

Lastly, we examined if the particle growth inferred from the PPS observations could be due to diffusive growth of the crystals. We multiplied the growth rate per crystal by the sedimentation lifetime. We found that 0.2-μm particles will grow to 0.25 μm in radius in the time it takes for them to fall out of the stratosphere. However, in our model most of our growth occurs in the upper levels where the species can first condense, in disagreement with the PPS findings. What could be happening is that ethane is condensing upon the acetylene and higher order hydrocarbon ice particles, causing them to grow in radius at higher pressures. If this is occurring then our calculated column densities are too large since we assume that each species condenses only on its own ice crystals. However, to properly solve this problem we need to compare the diffusive growth rate to the coagulation growth rate. Coagulation growth must be important because the time it would take for a haze particle to grow from 0.1 to 0.2 μm by diffusive growth is 120 years, 3 times longer than it would take the 0.1-μm particle to fall out. Thus to examine properly the question of haze particle growth requires a full microphysical model and is outside the scope of this work.

IV.B.2. Voyager IRIS. Ethane, acetylene, and diacetylene ices exhibit absorption bands in the spectral range covered by the IRIS spectrometer aboard Voyager 2 (10- to 50-μm). Characteristic absorption features occur at 304, 816, and 825 cm^{-1} for C_2H_6 ice (Leroi 1970, Pearl *et al.* 1991); 760 and 772 cm^{-1} for C_2H_2; and 223, 251, 653, and 663 cm^{-1} for C_4H_2 (Khanna *et al.* 1988). Unfortunately, no spectroscopic data on C_3H_6 and C_3H_8 ices has been published in the literature to our knowledge. Thus we could not search for their presence in the IRIS data.

Accordingly, we searched for possible signatures from C_2H_6, C_2H_2, and C_4H_2 ices in the thermal spectrum of Neptune, using the large average of 2920 IRIS spectra selected by Bézard *et al.* (1991). No feature exceeding the 3σ noise level can be seen in this spectrum at any of the expected locations. This nondetection can still be used to set upper limits on the haze column densities and thus constrain photochemical models.

We computed synthetic spectra of Neptune which included absorption by haze particles to determine the maximum haze density consistent with the lack of spectral features in the IRIS selection. In the absorption bands scattering is negligible compared to absorption because the range of particle radii considered for the photochemi-

cal hazes ($a \leq 1$ μm) is much smaller than the wavelength ($\lambda \geq 10$ μm). We have calculated the absorption cross sections from Mie theory, assuming that the particles are spherical. In the Rayleigh approximation ($a \ll \lambda$) valid here, the haze optical depth, τ_{haze}, is proportional to the total volume of the haze particles,

$$\tau_{haze} = \left(2\pi N_{crys}\frac{V}{\lambda}\right)\frac{18nk}{(n^2 + 2 - k^2)^2 + (2nk)^2} \quad (14)$$

where V is the volume of the sphere, λ the wavelength, n the real part of the refractive index, and k the imaginary part (Van de Hulst 1957). From Table VI and Eq. (14) it can be deduced that this opacity increases with decreasing particle radius. We then considered the most favorable situation for detection, particles having 0.1 μm radius, as a nominal case for our spectral calculations. The H_2–H_2 and H_2–He opacity is modeled as in Bézard *et al.* (1991). The temperature profile used in the calculations is the nominal egress profile shown in Fig. 1.

We calculated the absorption due to the 304-cm^{-1} ethane absorption band using recent laboratory measurements of the extinction coefficient (Dellarosa, personal communication, 1993). Ice crystals were assumed to be uniformly mixed with gas between the condensation level and the tropopause. Although the predicted column density for 0.1-μm particles is rather large, the emission feature produced in the Neptune synthetic spectra by the haze is extremely weak and well below the IRIS noise level. One reason is that this absorption band is intrinsically very weak, the absorption coefficient reaching at most 4 cm^{-1}. Another is that, the H_2–He continuum near 304 cm^{-1} originates from atmospheric levels near the tropopause, close to the location of the C_2H_6 haze, thus reducing the thermal contrast of the ethane feature. The 3σ upper limit for detection in the IRIS spectrum corresponds to a column density equal to 6×10^4 times that in the nominal haze model.

The ethane absorption features near 820 cm^{-1} cannot be detected in the IRIS spectrum regardless of the haze density. At this wavenumber, the noise equivalent temperature of the spectrum (i.e., the brightness temperature associated with the noise equivalent spectral radiance $\approx 4 \times 10^{-10}$ W cm^{-2} sr^{-1}/cm^{-1}) is $\approx$82 K. This is higher than the temperature where the C_2H_6 haze is expected to be located ($T \leq 64$ *K* see Table VI). Any spectral feature due to C_2H_6 ice would then be drowned in the instrument noise. This is also the case for the C_2H_2 feature at 760 cm^{-1} and the 653-, and 663-cm^{-1} features of C_4H_2; the noise equivalent temperature of the IRIS spectrum at these wavenumbers is greater than the condensation temperatures.

We searched for C_4H_2 absorption features at 223 and 251 cm^{-1}. Values for the complex refractive indices of crystalline C_4H_2 were taken from Khanna *et al.* (1988). Figure 10 shows synthetic spectra calculated with particle densities enhanced by factors 10^4 and 3×10^4 relative to the results of Case B for 0.1-μm-radius particles ($N_{crys} = 2 \times 10^6$ cm^{-2}). These calculations are compared with a no-haze spectrum (thick line). Since the model provides only constraints on the column density, two extreme distributions of haze particles with height were investigated. In the first one, haze particles are assumed to be uniformly mixed with gas within the haze formation region, i.e., only between the C_4H_2 and C_2H_2 condensation levels (dotted lines in Fig. 10). In this case, the haze opacity produces emission features since the haze temperature is higher than the tropospheric levels where the H_2–He continuum is formed. In the second case, we assumed that the C_4H_2 haze extends down to the tropopause region (solid thin lines). In this case, the bulk of the haze mass is located in the lower stratosphere where temperatures are lower than those of the H_2–He continuum. Absorption features are thus produced. The Voyager IRIS spectrum, shown for comparison, is systematically colder than the synthetic ones. This discrepancy may reveal the presence of thick tropospheric clouds (Conrath *et al.* 1991). The nominal C_4H_2 haze model yields a synthetic spectrum which is virtually indistinguishable from a no-haze calculation. It is thus consistent with the lack of absorption features at 223 and 251 cm^{-1} in the Voyager spectrum. We can only constrain the haze column density to be less than 2×10^9 particles cm^{-2}, i.e., 1000 times the nominal case, assuming that the C_4H_2 haze is distributed between the C_4H_2 and C_2H_2 condensation levels. In the alternate case in which the haze extends down to the tropopause, the 3σ upper limit is 2×10^{10} particles cm^{-2}. These constraints are even less stringent for larger particles.

IV.C. Comparison to Other Models

It is interesting to compare these results to the previous ones of Romani and Atreya (1989). They predicted a total stratospheric haze mass production rate of 4.2×10^{-15} g cm^{-2} sec^{-1}, of which 75% was ethane and 25% acetylene. They gave an overall factor of two uncertainty in the total haze mass production rate due to uncertainties in the eddy diffusion coefficient and methane mixing ratio. Despite changes in the K profile, CH_4 mixing ratio, photochemistry, and model atmosphere, ethane is still about 75% of the total haze mass production, and the total mass production rate is only 2.3 times higher than the preencounter prediction. The principal reason for the difference in the total haze mass production rates is that the ethane mass production rate in the preencounter model is only about half that of the current model rate. The acetylene in the preencounter model is 3.8 times the present model rate. Also,

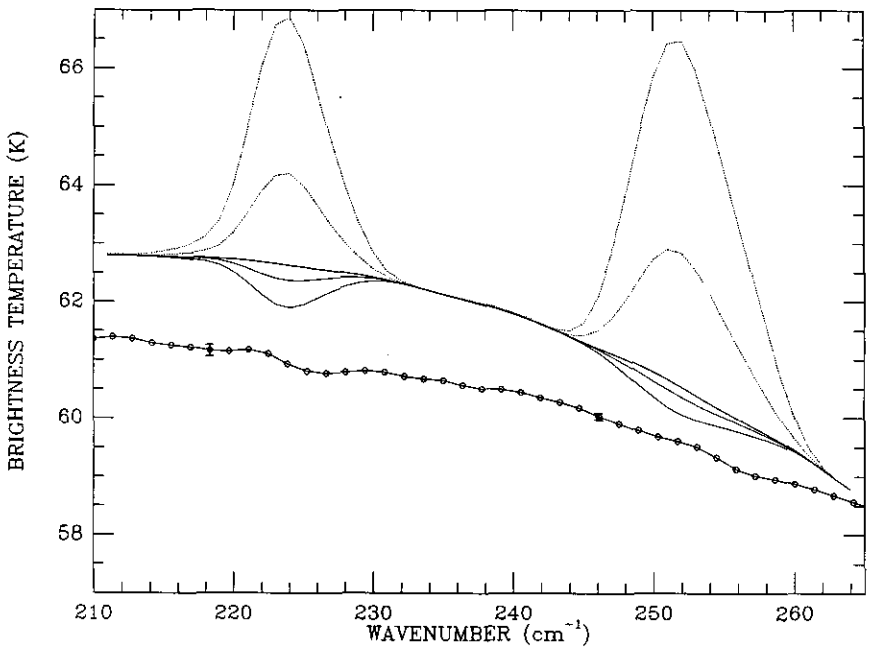

FIG. 10. Synthetic spectra calculated for the Case B model C_4H_2 haze with 0.1-μm particles and having column densities 10^4 and 3.0×10^4 times the column density in the nominal haze model (2.0×10^6 cm^{-2}). The thickest line is a no-haze spectrum. Dotted lines correspond to cases in which particles are uniformly mixed with gas between the C_4H_2 (90 km) and C_2H_2 (70 km) condensation levels. Thin solid lines correspond to cases in which particles are uniformly mixed with gas between the C_4H_2 condensation level (90 km) and the tropopause (50 km). A Voyager spectrum (average of 2920 individual spectra) is shown for comparison (line with dots). See text for discussion.

the preencounter model lacked the pathways to the C_3 and C_4 hydrocarbons and thus failed to predict the possibility of these hazes.

Moses *et al.* (1992) also examined haze formation from methane photolysis on Neptune. Like us, they used a one-dimensional photochemical model to predict the vapor phase abundances of the photolysis products of methane. The photochemical models are not identical; their model includes more C_3 and C_4 chemistry than ours (see Moses 1991), does not include a condensation loss process, and uses a different K profile (Eq. (9) with $\beta = 0.66$ and $K = 10^8$ cm^2 sec^{-1} at the CH_4 homopause) from the one we currently prefer. There is agreement between the two models that the haze is predominately ethane. However, their ethane production rate is about only 25% of ours. We note that their model is ethane poor compared to the IRIS results. The model C_2H_2 and C_4H_2 production rates agree well, but Moses *et al.* (1992) favor C_3H_8 and CH_3C_2H for the C_3 portion of the haze. We attribute the differences in predicted composition to the differences in chemistry and K profile used.

An important difference between the haze calculations is that Moses *et al.* (1992) calculate the necessary supersaturations to nucleate new ice haze particles while we assume that the ice crystals already exist. For acetylene and ethane we have found that once the ice crystals are present diffusive loss to them results in very low supersaturations ($\leq 10^{-2}$). For nucleation of new particles to continue the condensation nuclei must be efficient (see Table I, heterogeneous nucleation, Case A, in Moses *et al.* 1992, NB S = saturation, not supersaturation, s, and that $S = s + 1$). Alternatively, the condensation nuclei may not be efficient and the required supersaturations may be larger, e.g., 20–30 (From Table II, assuming heterogeneous nucleation). These supersaturations are higher by a factor $\geq$2000 than what we find at equilibrium for diffusive loss of the vapor to the crystals. We now discuss possible consequences if these larger supersaturations are needed to supply new ice crystals.

A straightforward way to increase the supersaturations calculated by the diffusive vapor loss model is to decrease the number density of crystals (see Eq. (8)). Since most of the vapor phase loss takes place in the first few levels once condensation starts, it is only necessary to decrease the number of crystals in this region (note that if we reduced the entire column density of crystals by the requisite amount the resulting haze burden would be much less than the derived PPS value). The consequence of this is that the haze particles are no longer distributed with the gas scale height throughout the entire haze area. Another way to increase the supersaturations is to lower the sticking efficiency (α in Eq. (3)). We have assumed this to be

unity—every vapor phase molecule that strikes an ice crystal sticks to it. This is the case for water well below the triple point, but at temperatures closer to the triple point it drops to ≈0.035 (Pruppacher and Klett 1980). The acetylene and ethane hazes are forming below their respective triple points (C_2H_6–90 K, C_2H_2–192 K, Ziegler 1959) which is why we chose 1.0 as a nominal value. However, water is more polar and thus more "sticky" than either C_2H_6 or C_2H_2. If we reduce α to 0.01 (representative of the lowest measured values for water, Pruppacher and Klett (1980) then for acetylene the supersaturations are now large enough that both nucleation of inefficient condensation nuclei and diffusive growth of existing ice crystals may take place at the same time. The supersaturations for ethane are still too low for this. We can, of course, use combinations of decreased α and the number density of crystals to raise the supersaturations. As an example, with $\alpha = 0.01$ and the ethane ice crystal number density reduced by a factor of 1000, the ethane supersaturations are finally large enough to support simultaneously inefficient nucleation and diffusive loss.

It is of course possible that high supersaturations are needed to nucleate new embryos but that once the ice crystals are formed low supersaturations result. This suggests episodic haze formation: the hazes nucleate, the supersaturations are reduced by diffusive loss of the vapor phase material onto the ice crystals, haze nucleation shuts off, the haze particles grow and settle out of the lower stratosphere, the supersaturations build up again, nucleation of new particles takes place, etc. The resupply time (from eddy diffusion) for C_2H_2 and C_2H_6 vapor into their respective condensation regions is longer (≈60 years) than the sedimentation lifetime for 0.2-μm-radius particles (≈14 years). Thus, it is possible for the hazes to snow out before the condensation region can be resupplied with new vapor phase material. A possible indication that this takes place is that Baines and Hammel (1992) find a latitudinal variation in the stratospheric aerosol burden. While their global average values agree well with Pryor *et al.* (1992), they find that in the equatorial region the haze column density must be 7.7 times smaller than the global average. We caution that this conclusion is speculative and beyond the limit of the simple steady-state model used here. At a minimum, a time-dependent model that includes detailed cloud microphysics directly into the photochemical model is needed.

V. SUMMARY/FUTURE WORK

With our methane photochemistry model we are able to reproduce well the global average Voyager IRIS C_2H_2 and C_2H_6 emission features. We have been less successful in simulating the Voyager UVS occultation lightcurves. In our modeling we have obtained the following constraints on the altitude profile of the eddy diffusion coefficient, K:

1. K varying with the atmospheric number density to some power produces poor model agreement with both the UVS and the IRIS data.

2. K must be low in the lower stratosphere (≈2 x 10^3 cm^2 sec^{-1} for pressures greater than ≈2 mbar), yet high in the upper stratosphere (>5 × 10^7 cm^2 sec^{-1} for pressures less than ≈0.5 mbar). This implies a well-mixed upper stratosphere overlying a stagnant lower stratosphere and a rapid transition between the two regions.

The second K profile improves the model fit because with it C_2H_2 and C_2H_4 are mixed rapidly from their sources at low pressures ($p \approx 10^{-3}$ mbar) to their sinks at high pressures ($p \approx 0.5$ mbar), which reduces the model mixing ratios as required by the data; yet the rapid mixing cannot extend to much higher pressures or C_2H_6, which is chemically inert, will be depleted below the abundance required by the data. For ethylene the most important sink is C_2H_4 + H (R63) and the model is sensitive to the rate constant for this reaction. The effect of this reaction is to convert ethylene to ethane before it can be photolyzed to acetylene. To obtain good agreement with the IRIS observations we must use the upper limit for this rate constant, and if we use twice the upper limit we can reproduce the IRIS emission features to within the noise uncertainties. The high-pressure sink for acetylene is conversion to vinyl (R62), which has an important three-body loss with methyl to form propene (R22). The major caveat in deriving the K profile from observations of acetylene and ethane is that the C_2H_2 and C_2H_6 mixing ratio profiles are dependent not only upon K, but the photochemical reaction scheme as well. Thus the above constraints on the K profile are subject to revision, if necessary, due to improved laboratory measurements of the photochemical reactions.

We then compared model haze results from the cases which best reproduced the IRIS and UVS vapor phase observations to IRIS and PPS constraints on the stratospheric haze. For solar maximum fluxes (Voyager encounter conditions) the model predicts a total aerosol mass production rate of hydrocarbon ices of 1 × 10^{-14} g cm^{-2} sec^{-1}, with haze formation occurring for temperatures ≤73 K. Ethane accounts for the majority of this, about 75% of the total haze production by mass, with C_2H_2 and C_3 and C_4 compounds making up the rest. The predicted location of the haze agrees with that derived from the PPS observations. However, balancing the above production rate by sedimentation for 0.25-μm-radius particles (PPS upper limit to particle radius) the predicted column density is 24% above the PPS upper limit to the haze burden. However, since both the eddy transport time of C_2H_2 and C_2H_6 vapor into the condensation region and the sedimentation lifetime of the haze particles

is longer than a solar cycle, the observed hazes are the result of production averaged over the solar cycle. For solar minimum conditions the model haze burden is below the PPS upper limit for 0.22-μm-radius aerosols. Thus, our model haze production is consistent with the PPS observations. We searched the IRIS spectra for a signature from these hazes but could only derive gross upper limits for the C_2H_6 and C_4H_2 hazes consistent with the predictions.

Our predicted supersaturations, which result from the diffusive vapor phase loss to already existing ice crystals, are on the order of 10^{-2} or less for acetylene and ethane in these cases. Moses *et al.* (1992) have shown that unless condensation nuclei are efficient higher supersaturations ($\gtrsim$20–30) are needed for these species for nucleation. It is possible to increase the supersaturations in the model to the point where nucleation on inefficient condensation nuclei can take place along with diffusive loss of the vapor. This will occur if the sticking efficiency of the vapor phase molecules to the ice crystals is $\leq$0.01. Another possibility is to have very few crystals in the levels where condensation first takes place because this is where the majority of the diffusive loss occurs. Of course, some combination of these two mechanisms is possible. Alternatively, haze formation on Neptune may be episodic since the diffusive loss process could reduce the supersaturations below the point where new haze particles could be nucleated.

Future work falls into three categories: model improvements, laboratory measurements, and more observations. Since the model indicates that C_3 and C_4 species are probably a significant portion of the haze, the corresponding chemistry in the model needs to be expanded. To better understand the haze formation and evolution process, more haze microphysics needs to be included in the photochemical model. To understand the interaction between nucleation and subsequent diffusive growth of the hydrocarbon ice crystals we need measurements of the sticking efficiency for conditions relevant to the lower stratosphere of Neptune. We encourage measurements of the reaction rates of $C_2H_4 + H$ and $CH_3 + C_2H_3$, as a function of pressure and temperature under conditions relevant to the stratosphere of Neptune. We could not find spectroscopic data for C_3H_6 and C_3H_8 ices, and thus could not search for their spectral signatures. Groundbased infrared observations of Neptune in the C_2H_4 or C_3H_4 bands at 949 and 748 cm^{-1}, respectively, would be useful to constrain the photochemical model. Since our preferred K profile implies nearly constant with height distributions of the C_2H_2 and C_2H_6 mixing ratios, observations from which the vertical profiles of these hydrocarbons could be retrieved would be a key test of the model.

ACKNOWLEDGMENTS

J.B. acknowledges support from NASA NAGW-1504 and NASA NASW-4806, SKA from NASA NAGW-1771. We would like to thank N. Dellarosa for use of the ethane ice absorption spectra prior to publication and W. Pryor for helpful conversations.

REFERENCES

ATREYA, S. K., J. BISHOP, AND P. N. ROMANI 1991a. Hydrocarbon abundances in the Neptune stratosphere: Latitudinal variations from Voyager UVS solar occultations. *EOS* **72,** No. 17 Supp. 185.

ATREYA, S. K., B. R. SANDEL, AND P. N. ROMANI 1991b. Photochemistry and vertical mixing. In *Uranus* (J. T. Bergstralh, E. D. Miner, and M. S. Matthews, Eds.), pp. 110–147. Univ. of Arizona Press, Tucson.

BAINES, K. H., AND W. H. SMITH 1990. The atmospheric structure and dynamical properties of Neptune derived from groundbased and IUE spectrophotometry. *Icarus* **85,** 65–108.

BAINES, K. H., AND H. B. HAMMEL 1992. The true blue nature of Neptune: The stratospheric methane abundance and properties of aerosols within the equatorial region as determined from ground-based CCD imagery. *Bull. Am. Astron. Soc.* **24,** 973.

BÉZARD B., P. N. ROMANI, B. J. CONRATH, AND W. C. MAGUIRE 1991. Hydrocarbons in Neptune's stratosphere from Voyager infrared observations. *J. Geophys. Res. Suppl.* **96,** 18,961–18,975.

BISHOP, J., S. K. ATREYA, P. N. ROMANI, B. R. SANDEL, AND F. HERBERT 1992. Voyager 2 UVS solar occultations at Neptune: Constraints on the abundance of methane in the stratosphere. *J. Geophys. Res. Planets* **97** 11,681–11,694.

BROADFOOT, A. L., S. K. ATREYA, J. L. BERTAUX, J. E. BLAMONT, A. J. DESSLER, T. M. DONAHUE, W. T. FORRESTER, D. T. HALL, F. HERBERT, J. B. HOLBERG, D. M. HUNTEN, V. A. KRASNOPOLSKY, S. LINICK, J. I. LUNINE, J. C. MCCONNELL, H. W. MOOS, B. R. SANDEL, N. M. SCHNEIDER, D. E. SHEMANSKY, G. R. SMITH, D. F. STROBEL, AND R. V. YELLE 1989. Ultraviolet spectrometer observations of Neptune and Triton. *Science* **246,** 1459–1466.

CONRATH, B. J., F. M. FLASAR, AND P. J. GIERASCH 1991. Thermal structure and dynamics of Neptune's atmosphere from Voyager measurements. *J. Geophys. Res. Suppl.* **96,** 18,931–18,939.

FAHR, A., A. LAUFER, R. KLEIN, AND W. BRAUN 1991. Reaction rate determinations of vinyl radical reactions with vinyl, methyl, and hydrogen atoms. *J. Phys. Chem.* **95,** 3218–3224.

FRENCH, R. G., P. A. MELROY, R. L. BARON, E. W. DUNHAM, K. J. MEECH, D. J. MINK, J. L. ELLIOT, D. A. ALLEN, M. C. B. ASHLEY, K. C. FREEMAN, E. F. ERICKSON, J. GOGUEN, AND H. HAMMEL 1985. The 1983 June 15 occultation by Neptune. II. The oblateness of Neptune. *Astron. J.* **90,** 2624–2638.

GLADSTONE, G. R. 1983. *Radiative Transfer and Photochemistry in the Upper Atmosphere of Jupiter.* Ph.D. thesis, California Institute of Technology.

HAMMEL, H. B., K. H. BAINES, AND J. T. BERGSTRALH 1989. Vertical aerosol structure of Neptune: Constraints from center-to-limb profiles. *Icarus* **80,** 416–438.

HINSON, D. P., AND J. A. MAGALHÃES 1993. Inertio-gravity waves in the atmosphere of Neptune. *Icarus* **105,** 142–161.

HOLTON, J. R., AND M. R. SCHOEBERL 1988. The role of gravity wave generated advection and diffusion in transport of tracers in the mesosphere. *J. Geophys. Res.* **93,** 11,075–11,082.

HUBBARD, W. B., J. E. FRECKER, J.-A. GEHRELS, T. GEHRELS, D. M. HUNTEN, L. A. LEBOFSKY, B. A. SMITH, D. J. THOLEN, F. VILAS, B. ZELLNER, H. P. AVEY, K. MOTTRAM, T. MURPHY, B. VARNES, B. CARTER, A. NIELSEN, A. A. PAGE, H. H. FU, H. H. WU, H. D. KENNEDY, M. D. WATERWORTH, AND H. J. REITSEMA 1985. Results

from observations of the 15 June 1983 occultation by the Neptune system. *Astron. J.* **90,** 655–667.

HUBBARD, W. B., P. D. NICHOLSON, E. LELLOUCH, B. SICARDY, A. BRAHIC, F. VILLAS, P. BOUCHET, R. A. MCLAREN, R. L. MILLIS, L. H. WASSERMAN, J. H. ELIAS, K. MATTHEWS, AND C. PERRIER 1987. Oblateness, radius, and mean stratospheric temperature of Neptune from the 1985 August 20 occultation. *Icarus* **72,** 635–646.

HUNTEN, D. M. 1975. Vertical transport in atmospheres. In *Atmospheres of Earth and the Planets* (B. McCormac, Ed.), pp. 59–72. Reidel, Dordrecht.

KHANNA, K. H., M. J. OSPINA, AND G. ZHAO 1988. Infrared band extinctions and complex refractive indices of crystalline C_2H_2 and C_4H_2. *Icarus* **73,** 527–535.

KOSTIUK, T., P. ROMANI, F. ESPENAK, AND B. BÉZARD 1992. Stratospheric ethane on Neptune: Comparison of ground-based and Voyager IRIS retrievals. *Icarus,* **99,** 353–362.

LAUFER, A. H., E. P. GARDNER, T. L. KWOK, AND Y. L. YUNG 1983. Computations and estimates of rate coefficients for hydrocarbon reactions of interest to the atmospheres of the outer solar system. *Icarus* **56,** 560–567.

LEE, J. H., J. V. MICHAEL, W. A. PAYNE, AND L. J. STIEF 1978. Absolute rate of the reaction of atomic hydrogen with ethylene from 198 to 320 K at high pressure. *J. Chem. Phys.* **68,** 1817–1820.

LEROI, G. E. 1970. *Vibrational Spectra of Simple Molecular Crystals.* Presented at the national meeting of the American Crystallographic Association, New Orleans, LA.

LIGHTFOOT, P. D., AND M. J. PILLING 1987. Temperature and pressure dependence of the rate constant for the addition of H to C_2H_4. *J. Phys. Chem.* **91,** 3373–3379.

LINDAL, G. F. 1992. The atmosphere of Neptune: An analysis of radio occultation data acquired with Voyager 2. *Aston. J.* **103,** 967–982.

LINDAL, G. F., J. R. LYONS, D. N. SWEETNAM, V. R. ESHLEMAN, D. P. HINSON, AND G. L. TYLER 1990. The atmosphere of Neptune: Results of the radio occultation measurements with the Voyager 2 spacecraft. *Geophys. Res. Lett.* **17,** 1733–1736.

LINDZEN, R. S. 1971 Tides and gravity waves in the upper atmosphere. In *Mesospheric Models and Related Experiments* (G. Fiocco, Ed.), pp. 122–130. Reidel, Dordrecht.

LINDZEN, R. S. 1981. Turbulence and stress owing to gravity wave and tidal breakdown. *J. Geophys. Res.* **86,** 9707–9714.

MARRERO, T. R., AND E. A. MASON 1972. Gaseous diffusion coefficients. *J. Phys. Chem. Ref. Data* **1,** 3–118.

MARTEN, A., D. GAUTIER, T. OWEN, D. SANDERS, H. E. MATTHEWS, S. K. ATREYA, R. J. P. TILANUS, AND J. DEANE 1993. First observations of CO and HCN on Neptune and Uranus at millimeter wavelengths and their implications for atmospheric chemistry. *Astrophys. J.* **406,** 285–297.

MORDAUNT, D. H., I. R. LAMBERT, G. P. MORLEY, M. N. R. ASHFOLD, R. N. DIXON, C. M. WESTERN, L. SCHNIEDER, AND K. H. WELGE 1993 Primary product channels in the photodissociation of methane at 121.6 nm. *J. Chem. Phys.* **98,** 2054–2065.

MOSES, J. I. 1991. *I. Phase Transformations and the Spectral Reflectance of Solid Sulfur: Possible Metastable Sulfur Allotropes on Io's Surface. II. Photochemistry and Aerosol Formation in Neptune's Atmosphere.* Ph.D. thesis, California Institute of Technology.

MOSES, J. I., Y. L. YUNG, AND M. ALLEN 1992. Hydrocarbon nucleation and aerosol formation in Neptune's atmosphere. *Icarus* **99,** 318–346.

ORTON, G. S., AND J. F. APPLEBY 1984. Temperature structure and infrared-derived properties of the atmospheres of Uranus and Neptune. In *Uranus and Neptune* (J. T. Bergstralh, Ed.), pp. 89–156. NASA Conference Publication 2330.

ORTON, G. S., K. H. BAINES, J. CALDWELL, P. ROMANI, A. T. TOKUNAGA, AND R. A. WEST 1990. Calibration of the 7- to 14-μm brightness spectra of Uranus and Neptune. *Icarus* **85,** 257–265.

ORTON, G. S., H. H. LACY, J. M. ACHTERMANN, P. PARMER, AND W. E. BLASS 1992. Thermal spectroscopy of Neptune: The stratospheric temperature, hydrocarbon abundances, and isotopic ratios. *Icarus* **100,** 541–555.

PARKINSON, C. D., J. C. MCCONNELL, B. R. SANDEL, R. V. YELLE AND A. L. BROADFOOT 1990. He 584 Å Dayglow at Neptune. *GRL,* **17,** 1709–1712.

PEARL, J., M. NGOH, M. OSPINA, AND R. KHANNA 1991. Optical constants of solid methane and ethane from 10,000 to 450 cm^{-1}. *J. Geophys. Res.* **96,** 17,477–17,482.

PRUPPACHER, H. R., AND J. D. KLETT 1980. *Microphysics of Clouds and Precipitation.* Reidel, Dordrecht.

PRYOR, W. R., R. A. WEST, K. E. SIMMONS, M. DELITSKY 1992. High phase angle observations of Neptune at 2650 Å and 7500 Å: Haze structure and particle properties. *Icarus* **99,** 302–317.

REID, R. C., J. M. PRAUSNITZ, AND T. K. SHERWOOD 1977. *The Properties of Gases and Liquids.* McGraw–Hill, New York.

ROMANI, P. N., AND S. K. ATREYA 1989. Stratospheric aerosols from CH_4 photochemistry on Neptune. *Geophys. Res. Let.* **16,** 941–944.

ROMANI, P. N., AND S. K. ATREYA 1988. Methane photochemistry and haze production on Neptune. *Icarus* **72,** 424–445.

ROQUES, F., B. SICARDY, R. G. FRENCH, W. B. HUBBARD, A. BARUCCI, P. BOUCHET, A. BRAHIC, J.-A. GEHRELS, T. GEHRELS, I. GRENIER, T. LEBERTRE, J. LECACHEUX, J. P. MAILLARD, R. A. MCLAREN, C. PERRIER, F. VILAS, M. D. WATERWORTH 1992. Neptune's upper stratosphere, 1983–1990 ground-based stellar occultation observations. III. Temperature profiles. Submitted for publication.

STROBEL, D. F., M. E., SUMMERS, F. HERBERT, AND B. R. SANDEL 1990. The photochemistry of methane in the atmosphere of Triton. *GRL* **17,** 1729–1732.

SUMMERS, M. E., AND D. F. STROBEL 1989. Photochemistry of the atmosphere of Uranus. *Atrophys. J.* **346,** 495–508.

VAN DE HULST, H. C. 1957. *Light Scattering by Small Particles.* Wiley, New York.

YELLE, R. V., F. HERBERT, B. R. SANDEL, R. J. VERVACK, JR., AND T. M. WENTZEL 1993. The distribution of hydrocarbons in Neptune's upper atmosphere. *Icarus* **104,** 38–59.

ZIEGLER, W. T. 1959. *The Vapor Pressures of Some Hydrocarbons in the Liquid and Solid State at Low Temperatures.* National Bureau of Standards Technical Note 4.